



Geomorphological, hydrogeological and geotechnical characteristics of the El Kherba large, deep-seated landslide induced by the August 7th, 2020 (Mw 4.9) earthquake in the city of Mila, northeast Algeria

Hamid Bourenane¹ · Nourredine Mezouar¹

Received: 5 December 2023 / Accepted: 24 May 2024 / Published online: 26 June 2024
© The Author(s) 2024

Abstract

The present research study aims to create accurate and comprehensive inventory mapping while investigating the geomorphological and geotechnical characteristics of the large, deep-seated, and damaging El Kherba landslide triggered by the August 7, 2020 (Mw 4.9) Mila earthquake. The methodology relies on the analysis of results obtained through detailed field investigations, satellite image interpretation, deep boreholes equipped with piezometers, laboratory tests, in situ tests, and numerical simulations. The resulting landslide inventory map reveals a significant earth slide with an active zone covering a surface area of 1.565 km², extending approximately 2,166 km in length, with a width ranging from 40 m to 1.80 km, and a volume of 25,784,909 m³. Geomorphological field mapping results revealed a large and deep-seated morphological deformation related to: (i) the weak mechanical resistance and low stability slopes that the seismic strengths caused a reduction in the shear strength of the soil; (ii) Miocene clays, highly altered and potentially subject to shrinkage and swelling; (iii) a partial reactivation of a previously existing large landslide; (iv) human activity such as slope excavation and unplanned urbanization; and (v) topographical and lithological site effects. The results of geological and hydrogeological investigations indicated the presence of: (i) thin and thick weak-resistance interlayers of altered and plastic clays with weak resistance, which may constitute shear surfaces; (ii) a shallow aquifer that impacted the mechanical resistance characteristics. Laboratory tests revealed that the fine clay in the soil was highly weathered, with a low dry density and a high moisture content, along with a high saturation and plasticity, making it very sensitive to the presence of water. Undrained triaxial cyclic loading tests indicated a high potential for the generation of excess pore-water pressures in the material during seismic loading. The direct shear test showed that the disturbed soils had an average cohesion of 33.4 kPa/m² and an internal friction angle of 18.21°, indicating poor structural and shearing strength. The results of the oedometer test indicated that the soils are compressible to highly compressible, overconsolidated, and have the potential for swelling. According to the Manard pressuremeter test (MPT) and available empirical relationships, the landslide exhibited a deep-seated nature, with sliding surfaces located along weak geotechnical characteristics interlayers at a depth ranging between 10 and 40 m. The depths of failure obtained from the MPT were consistent with those determined by the empirical relationships available in the literature and numerical simulations. This comprehensive research provides valuable data on earthquake-induced landslide and can serve as a guide for the prevention and mitigation of landslide risks.

Keywords Deep-seated landslide · Geotechnical condition · Seismic loading · Susceptibility factors · Numerical modeling

Introduction

Northern Algeria, located along the convergent plate boundaries between the African tectonic and Eurasian plates, is prone to frequent earthquakes and significant induced hazards. Earthquake-induced landslides, often associated with moderate-to-high magnitudes, pose a severe threat to both human lives and property (Benouar 1994; Guemache et al. 2009; Bouhadad et al. 2010; Hadji et al. 2013; Bourenane

✉ Hamid Bourenane
b.hamid@hotmail.com

¹ Seismic Microzonation Research Division, National Earthquake Engineering Research Center (CGS), 1 Rue Kaddour Rahim, Hussein Dey, Alger, Algeria

et al. 2014, 2016, Amar et al. 2021; Tebbouche et al. 2022). They are common and highly destructive, causing substantial economic losses every year and acting as a significant hindrance to the urban development and planning of numerous urban areas located in close proximity to the epicentral zones (Bouhadad et al. 2010; Amar et al. 2021; Bourenane et al. 2016; Bourenane et al. 2021; Bourenane et al. 2022; Bourenane 2023). Currently, the impact of landslides is increasing dramatically due to rapid and unplanned urbanization, poor environmental management, a lack of rules and regulations, the development of urbanization and infrastructure in unstable areas, and a lack of geotechnical studies for slope stability and characterization (Bourenane and Bouhadad 2021).

Deep-seated destructive landslides are large, rapid slope movements that are commonly accompanied by earth or rock avalanches, capable of causing extensive devastation over large areas. Severe earthquakes have proven to be catalysts for initiating a multitude of mass movements, exhibiting diverse sizes and scales. Studies, including Pederson et al. (1994), have observed that smaller landslides tend to concentrate on steep slopes and ridge tops, a phenomenon attributed to the amplification of seismic shaking. Conversely, larger and deeper-seated landslides are primarily influenced by the specific geological structure of the local area. The triggering of these slope movements is linked to the appearance of transient inertial forces that modify the equilibrium of slopes generally close to failure. These inertial forces result from the propagation of seismic waves through the slope, which are modified by its local topographical, geological, and geotechnical characteristics (Bourdeau 2005). Consequently, the occurrence, type abundance, and deformation mechanisms of earthquake-induced landslides in an area are complex and influenced by a combination of the geomorphological and lithological setting and the mechanical and hydrogeological properties of the rocks and soils (Rodriguez et al. 1999; Keefer 1984, 2002; Harp et al. 2011; Xu et al. 2013; Huang et al. 2018). Therefore, understanding the mechanisms of specific landslides induced by such interactions is complex, requiring thorough investigation and the application of various reconnaissance methods. Geomorphological, geological, hydrogeological and geotechnical data from recent landslides play a crucial role in identifying potential landslide sites. Comprehensive studies of the geotechnical properties of lithological units are fundamental for landslide prediction. Many deep-seated landslides triggered by earthquakes or rainfall can be anticipated through slope deformation; understanding geomorphic consequences, such as depressions and scarplets, aids in prediction efforts (Bourenane et al. 2022).

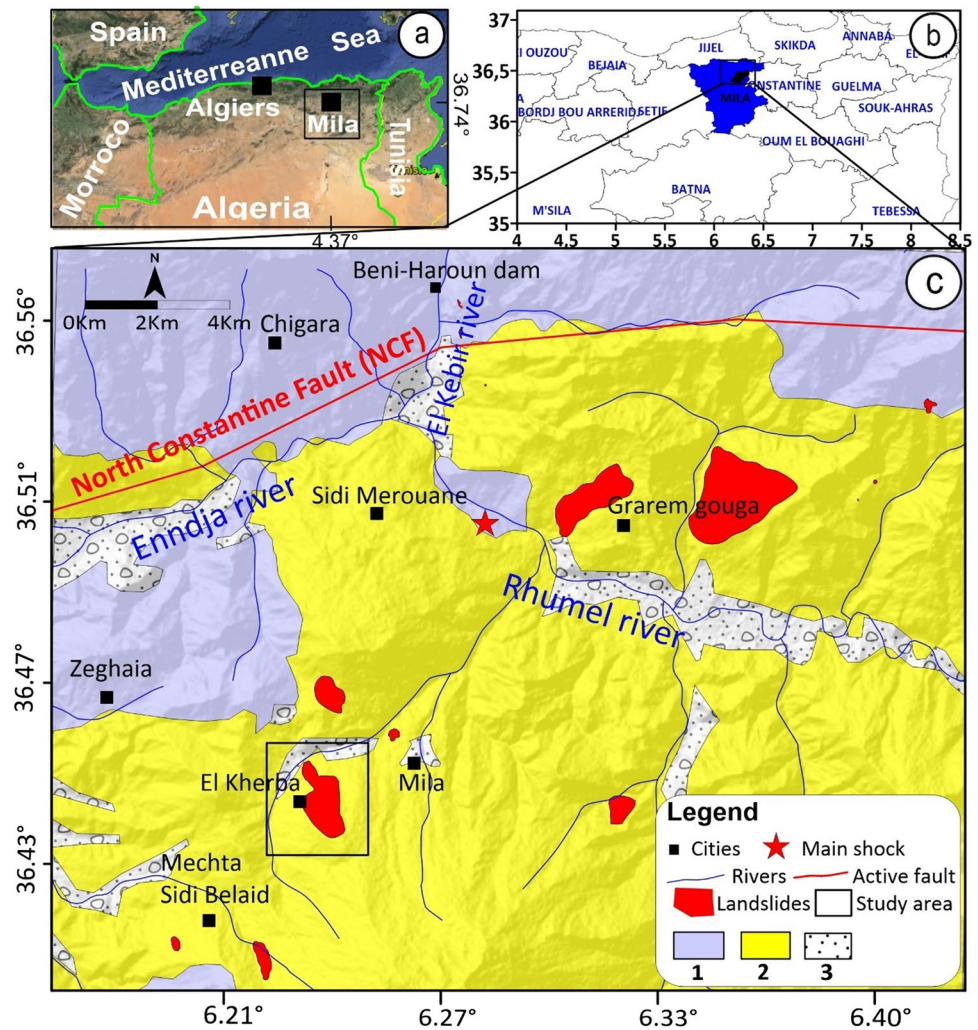
The recent earthquake of magnitude Mw 4.9 (CRAAG 2020) that struck the province of Mila on August 7th, 2020, at 7:15 a.m. local time, triggered numerous and diverse types of landslides over an area of about 500 km² (Fig. 1), despite

its relatively small size. The landslides resulted in significant damage to settlements, including the collapse of constructions, leaving hundreds of people homeless, especially in El Kherba city. The El- Kherba landslide is one of the most damaging, complex, and large deep-seated landslides triggered by this event in the western part of the city of Mila (Fig. 2). The ongoing landslide resulted in significant harm to numerous buildings and infrastructure, leading to substantial ground deformation in highly vulnerable areas near El Kherba, El Amel, and Kandahar districts. It affected more than 1,055 constructions, including a primary school, a middle school, roads, and two water supply reservoirs with a capacity of 2 * 15,000 m³, were affected (Fig. 2). Currently, the El Kherba landslide constitutes an important risk, representing a significant cause for concern and, therefore, a high-priority scientific challenge due to its location in urban zones, its surface area, and the extent of the induced disorders. The main causes of these disorders are not related to the quality of the structures or construction materials used in construction. Instead, they can be attributed to the instabilities of the underlying foundation soils, which were not identified in the previous geotechnical studies.

In numerous studies, researchers around the world have extensively discussed earthquake-induced landslides, recognizing that understanding their characteristics, controlling factors, and evolutionary mechanisms is a principal challenge and of valuable importance for landslide prediction, control, monitoring, and providing essential data for identifying susceptibility analysis, hazard assessment, and risk reduction measures (e.g., Dai and Lee 2002; Dai and Lee 2002; Harp et al. 2011; Harp et al. 2011; Guzzetti et al. 2012; Bourenane et al. 2022). Furthermore, precise mapping and a thorough comprehension of the spatial distribution of coseismic landslides, along with the relationship between landslide occurrence locations and influencing factors, are vitally important for identifying and characterizing active faults (Xu and Xu 2014; Huang et al. 2018).

At present, a large amount of research has been carried out by local and international researchers to explore the main factors affecting landslide deformation, deepen the understanding of landslide deformation mechanisms, accurately predict landslide formation, and take timely, effective measures to prevent the occurrence of landslides. The factors affecting landslide deformation can be divided into susceptibility factors such as topography and geomorphology, stratigraphic structure, and geotechnical properties (Wang et al. 2010; Wang et al. 2012; Huang 2012; Tang et al. 2016; Su et al. 2017; Huang et al. 2018; Pasierb et al. 2019; Dai et al. 2019; Li et al. 2020; Shi et al. 2021; Chen et al. 2021; Zou et al. 2021; Xia et al. 2021; Bourenane et al. 2021, Bourenane et al. 2022; Bahmani et al. 2022; Wu et al. 2023; Ke et al. 2023) and, triggering factors such as heavy rainfall, groundwater level, and human engineering

Fig. 1 Geographical, geological and geomorphological setting of the study area: a) location within the north center of Algeria and Mila region at East of the capital city Algiers; b) administrative limit of the prefecture (Wilaya) and municipality of Mila; and c) inventory map of landslides triggered by the Mila earthquake obtained by visual interpretation of interferometry synthetic aperture radar (InSAR) satellite images and Google Earth satellite images completed by the field investigation after the 2020 Mila Earthquake and geological formations draped on the digital elevation model (DEM): 1. Sandstone and limestone (Oligocene), 2. Clays, marls and lacustrine limestones (Mio-Pliocene), 3. Scree and quaternary alluvium (Vila 1980; Meghraoui 1988; Coifait 1992). The red star indicates the Mila earthquake epicenter on August 7, 2020. The black square corresponds to the large deep-seated landslide of El Kherba in the west of Mila city



activities (Chen et al. 2012; Shoaei 2014; Zhu et al. 2019; Li et al. 2022; Zhang et al. 2021; Dong et al. 2022; Bourenane et al. 2021, 2022). Recently, several studies have investigated the landslide inventory and the spatial correlations between coseismic landslide distribution and control factors based on historical landslide inventories were performed (Rodriguez et al. 1999; Keefer 1984, 2002; Chong et al. 2013; Harp et al. 2011; Huang et al. 2018). The scholars investigated data from historical earthquake-induced landslides world-wide and obtained the minimum shaking intensities and threshold magnitudes for landslide occurrence and the statistical correlation between the maximum distances of landslides from the fault or epicenter for each type of landslide induced by an earthquake along with regression equations are developed and some adjustments on correlations are obtained.

From these researchs, multi-combination reconnaissance methods such as geomorphological and geological mapping, observation-based methods, as well as geophysical and geotechnical methods, were developed and became a promising approach for studying and characterizing

landslides. However, in recent decades, the knowledge of this phenomenon has become more detailed and comprehensive as increased resources and new surveying tools, such as aerial photography, Geographic Information Systems (GIS), and remote sensing technologies, have become available. The majority of research on this topic focuses on major earthquakes; moderate-sized earthquakes can also cause considerable slope failure, but related studies are few. Moreover, most of the research is qualitative, which is still lacking, and the quantitative analysis of influencing factors is still on the surface, which leads to the inability to accurately determine the degree of influencing factors on landslide deformation and reduces the accuracy and effectiveness of the prevention and control measures taken. In recent decades, based on field observations, improved remote sensing technology, and widely accepted landslide-mapping methods, many extensive earthquake-induced landslide inventories have been generated for seismic events. For this lack, the use of combination methods is a promising approach

Fig. 2 Example of different damages of buildings and roads caused by El Kherba landslide caused by the August 7, 2020 earthquake event: **a**) total collapse of the structures in El- Kherba city, **b**) cracks in the masonry, **c**) and **d**) partial collapse of the buildings mainly due to the collapse of the soil. **e**) bursting of the house due to the landslide at El Amel city, **f**) collapse and horizontal displacement of the road, **g**) cracks and the opening of the rupture joint in the water tower near the headscarp



allowing better qualitative and quantitative analysis of landslides, particularly on a large scale.

Following the El Kherba-induced landslide, the National Laboratory for Housing and Construction (LNHC 2020) conducted a comprehensive geotechnical study as part of a specific investigation into the landslide. This study contributed significantly to characterizing the landslide by identifying the presence of sliding surfaces through inclinometer and piezometer investigation campaigns. Regardless of the obtainability of interesting geotechnical data, the internal structure, deformation characteristics, causal factors, and evolution mechanism of the landslide remain unknown. In addition, inclinometer results are subject to ambiguity and do not provide a clear position of the sliding surface.

Therefore, a comprehensive approach involving of geomorphological mapping based on detailed field geological survey and remote-sensing techniques combined with geological, geotechnical, and hydrogeological data becomes crucial in this structural context, especially when identifying deformations, which mark different stages of its evolution mechanism.

This paper thus investigates a detailed geomorphological, geotechnical and hydrogeological characteristic, with the identification of the failure mechanism of the El- Kherba landslide induced by the Mila earthquake (Mw 4.9) based on the combinaison of field investigation, remote sensing images interpretation, and analysis of laboratory and in-situ geotechnical test data and

hydrogeological monitoring data. The final objective is to improve existing earthquake induced landslide susceptibility methods based on casual relationships between landslides geo-environmental and triggering factors during earthquake. The findings offer improved insights into the triggering and susceptibility mechanisms of potential landslide sites and thus contribute to the development of a methodology for predicting potential sites and guiding the scientific disaster prevention and mitigation work of this landslide and similar landslides.

Description of the investigated area

Geographical setting

The triggered landslide under investigation occurred in the west part of the city of Mila (northeast Algeria) along the right bank of the El Kherba river, approximately 390 km east of Algiers, the capital of Algeria (Fig. 2a), and about 2 km west of the Mila municipality (Fig. 2b). It is delimited by its geographical coordinates: longitudes of 6.225°N and 6.258°N and latitudes of 36.431° E and 36.456° E, referenced to WGS 1984 and UTM Zone 32, North. Most of the local landslide is located within a discontinuous urban area and covered by a sparsely vegetated area in the agricultural land. The area, densely populated within the city of Mila, exhibits the most favorable geomorphological, hydrogeological, and geotechnical conditions for such occurrences.

Geomorphological, geological, and climatic setting

Geomorphologically, the Mila province belongs to the great Mila-Constantine Neogene basin, which corresponds to a vast and closed depression intra-mountain covered by Neogene deposits overlying a substratum consisting of generally allochthonous flysch nappes. The affected zone lies in a hilly area within the western part of the larger Mila-Constantine basin. It is located in a transition zone between the Numidian Mountain chain in the north and the high plains of Constantine in the south (Fig. 2a). Moderately sloped hills with a maximum height less than 800 m a.s.l. and an average elevation of 500 m a.s.l. dominate the area's morphology. The El Kherba landslide is localized in low- to middle-elevation hills with a slope dipping northwest at an angle of 10 to 30°. The upper slope of the landslide is gentler than the lower one. The elevation ranges from 400 to 680 m above sea level and increases from the northwest to the southeast. The head of the landslide occurred at an altitude of 700 m near the water tower, and the landslide toe is at an elevation of 400 m near the El-Kherba River.

Geologically, the epicentral area is part of the Mila-Constantine Neogene basin, located in the internal zones of the Maghrebides chain (Coiffait 1992), exhibiting four main lithological formations (Fig. 2c): (1) Triassic evaporites and Jurassic carbonate formations; (2) Cretaceous marls and marly limestones underlying Paleocene–Eocene marls; (3) Mio-Pliocene formations cover most of the Mila basin, represented by detrital deposits (conglomerates, sands, and clays), evaporitic deposits (gypsum, anhydrite, and rock salt), and lacustrine limestones; and (4) Quaternary alluvial terraces and lacustrine calcareous formations (Vila 1980; Coiffait 1992).

The Neogene clays and marl formations of the Mila-Constantine Neogene basin are the dominant formation types (Coiffait 1992) that cover a large surface of the landslide site and exhibit weak geotechnical characteristics (Athmania et al. 2010; Chettah 2008): low shear strength and cohesion, high sensitivity to the presence of water, and high plasticity and swelling. Consequently, these formations are highly susceptible to landslides.

The Mila region is located at the junction of two different climatic domains: (i) a temperate and humid climate in the North, characterized by a dry and hot summer and a mild and wet winter with annual precipitation ranging between 900 and 1200 mm; and (ii) a semi-arid climate in the South, marked by a significant temperature difference (40 °C in summer and can fall below 0° C in winter) and precipitation of about 400 mm/year. In the winter season, there is a rise in both the frequency and intensity of rainfall, characterized by highly variable precipitation amounts (700 to 1000 mm. yr⁻¹), posing a landslide risk. A period of reduced rainfall, also known as the dry season, is observed in August, the period when the El Kherba landslide occurred.

From a hydrological point of view, the Mila province belongs to the watershed hydrographic basin of Kebir-Rhumel, characterized by a very dense hydrographic network. It is drained by the El Kebir, Rhumel, and Enndja rivers with a permanent flow and very active seasonal flows in the winter period, which are associated with temporary flow affluents: Oued Mila, Oued Makraoued, Oued El Bordjia, and Oued El Kotone (Fig. 2c). These watercourses are likely to be the origin of floods and other forms of instability on the slopes, causing damage, sometimes considerable, to different parts of the infrastructure of the city. The topographic profile in an east–west direction confirms this hilly morphology with a dense hydrographic network and clearly visible differential erosion. In specific locations within the region, such as El Kherba, gullies form along drainage courses due to heavily weathered and erodible soil. This local phenomenon significantly contributes to the instability of the natural slopes in the area. The region's hydrogeology is mainly

governed by the repartition of impermeable Miocene clays and marls underlain by permeable Pliocene lacustrine limestone and Quaternary alluvial terraces.

The gradual extension of urban areas due to rapid urbanization from 1962 until today, accompanied by human activity developments, has resulted in significant morphological changes and modifications of stability conditions in the Mila province. These changes, including excavation, extensive clear-cut logging, and vegetation removal, constitute the main factors contributing to the increased frequency of landslides. El Kherba is among the cities experiencing forced urbanization in landslide-prone areas due to the rapid population increase in Mila municipality. As a result of this growth, new developments combined with inappropriate land use practices are the main factors responsible for the increased frequency of landslides.

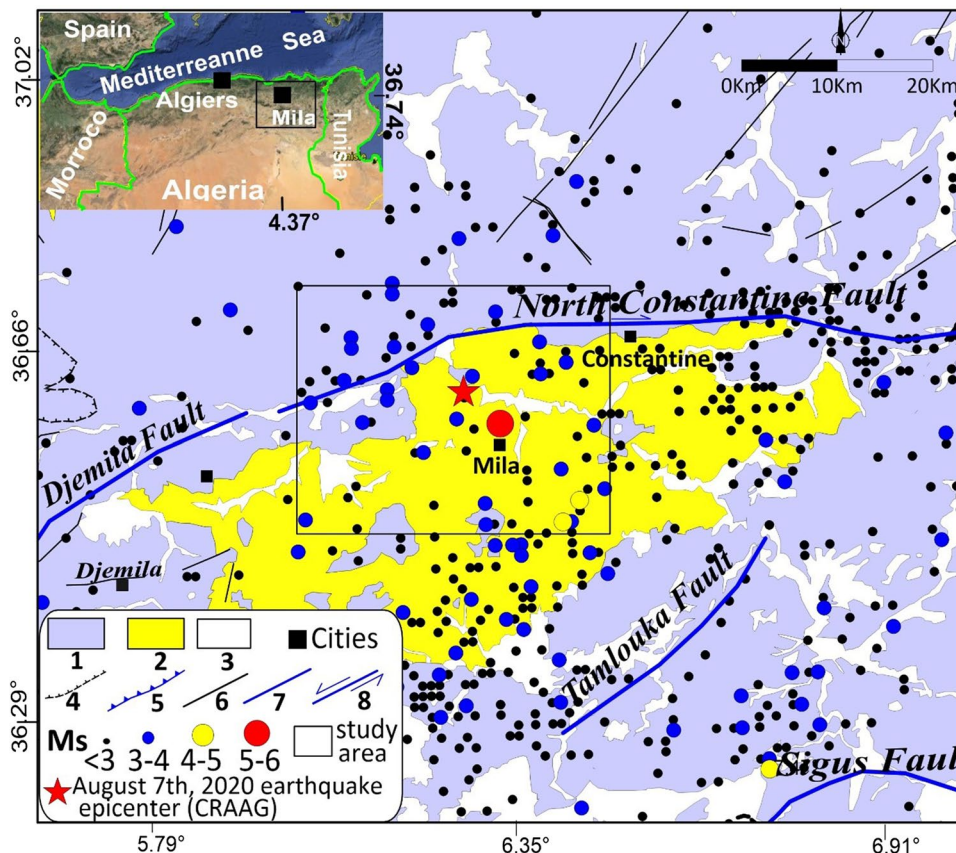
The seismotectonic setting

The Eastern Tell Atlas of Algeria is situated in a complex deformation zone caused by the collision between the Eurasian plate and the African tectonic plate. This plate boundary zone is controlled by left-lateral strike-slip movement and compression at a rate of about 2.4 mm/yr, with the African plate moving toward the Eurasian plate

in the northwest direction (Sato et al. 2007; Bougrine et al. 2019). This region is distinguished by three major fault systems, which include (Fig. 3): (i) reverse faulting and right lateral strike slip due to NE-SW to E-W trending faults (Bounif et al. 1987; Meghraoui 1988; Bouhadad et al. 2003; Maouche et al. 2011, 2019); (ii) left lateral faulting due to NW–SE oriented faults (Beldjoudi et al. 2016), and even (iii) normal faulting in the Guelma basin (Aoudia et al. 2000). Several active faults have been described by various authors, including Vila (1980), Meghraoui (1988), Harbi et al. (1999), Bouhadad et al. (2003), and Maouche et al. (2011). Additionally, potentially active faults have been identified offshore north of Jijel, Annaba, and Skikda (Harbi et al. 1999, 2011). In terms of seismic hazard, several studies indicate that the eastern Algeria area has a relatively moderate seismic hazard (Aoudia et al. 2000; Kherroubi et al. 2009; Maouche et al. 2011).

The Mila province is situated in an active zone marked by moderate seismic activity in north-eastern Algeria (Fig. 3). It has historically experienced several moderate earthquakes, including: the Jijelli 1856 earthquake that caused a tsunami (Harbi et al. 2011), the 1946 Berhoum and the 1937 Guelma moderate-sized earthquakes (Benouar 1994); the Constantine October 27th, 1985 (Mw 5.7) earthquake (Bounif et al.

Fig. 3 Seismotectonic map of eastern Algeria (Vila 1980; Meghraoui 1988; Bounif et al. 1987; Bouhadad et al. 2003; Kherroubi et al. 2009). The seismicity data are from (Harbi et al. 2004; Ayadi and Bezzeghoud 2015). 1. Sandstone and limestone (Oligocene), 2. Clays, marls and lacustrine limestones (Mio-Pliocene), 3. Scree and quaternary alluvium, 4. hidden faults, 5. faults, 6. active faults, 7. Strike-slip (Vila 1980; Meghraoui 1988; Bounif et al. 1987). The red star indicates the Mila earthquake epicenter on August 7, 2020



1987); the Beni Ourtilane November 20th, 2000 (Mw 5.4) earthquake (Bouhadad et al. 2003); the Beni Ilmane earthquakes sequence of May 2010 (Beldjoudi et al. 2016); the Laalam earthquake of Mars 20, 2006 (Bouhadad et al. 2010); and recently, the July–August 2020 earthquakes of Mila with a magnitude of Mw = 4.6 and Mw = 4.9, respectively (Amar et al. 2021).

The recent earthquakes in July–August 2020 occurred along the North Constantine Fault (NCF), which is considered a major structural feature and corresponds to a structural limit between Neogene basins and pre-Neogene deposits (Vila 1980; CGS 2022). This fault zone contains a series of NE-SW to E-W trending fault segments totaling more than 50 km in length (CGS 2022). The NCF is a reverse fault with a low to moderate seismicity pattern (Fig. 3).

According to the CRAAG, the earthquake of August 7, 2020 (Mw 4.9) that hit the north of Mila province was felt in a vast portion of northeastern Algeria. The epicenter was located about 10 km NE of the city of Mila at latitude 36.56° and longitude 6.35°, with a focal depth of 8 km. Numerous felt aftershocks were recorded following the main event, with the strongest one being a 4.5-magnitude shake at 11:13 am local time on August 7, 2020 (Amar et al. 2021).

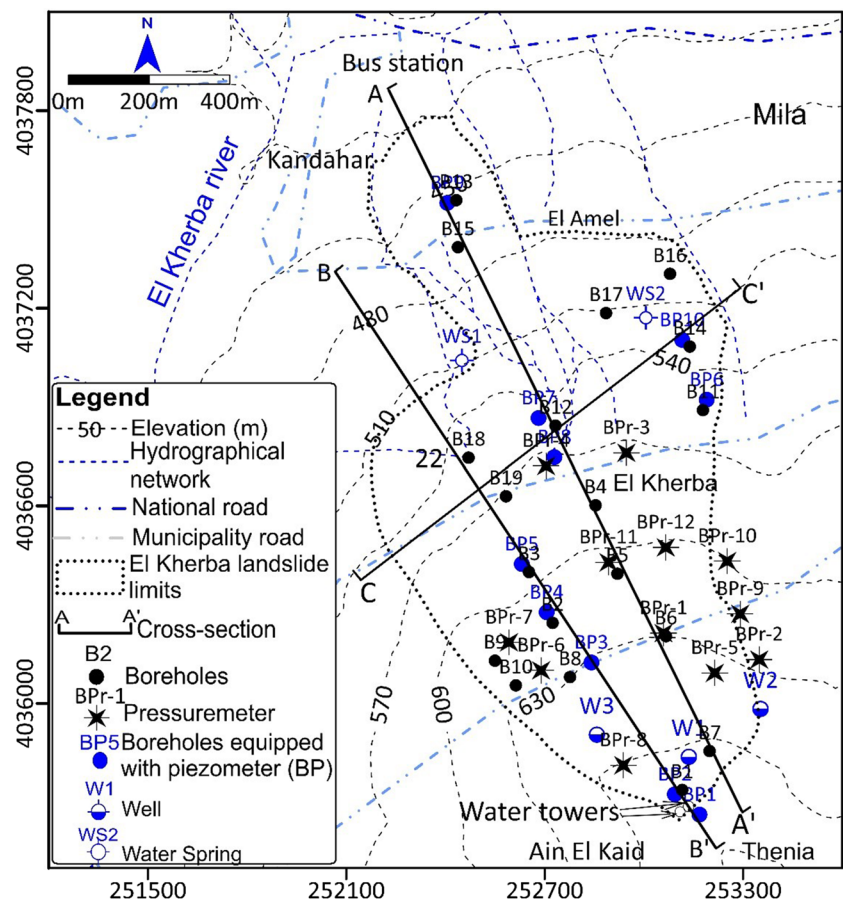
Investigation Data and methodology

Data types compilation and spatial database construction using GIS

To investigate the instability of El Kherba induced by the Mila earthquake, we compiled, analyzed, and processed data from geological, geotechnical, and hydrogeological investigation campaigns. Additionally, field investigations and satellite imagery interpretation were conducted. The gathered data were integrated into a database using the GIS framework, specifically ArcGIS and Access. This integration facilitated spatial analysis, exploitation, processing, and management of large datasets in the local projection system of Algeria (UTM North Sahara, 1959; WGS 1984; spindle 31 North). The compiled database, as illustrated in Fig. 4, includes:

- **Topographic Digital Data:** This encompasses elevation, slope gradient, slope aspect, and topographic position information, derived from an 8 m resolution Digital Elevation Model (DEM) created by digitizing and interpolating elevation lines from 1:25,000 topographic maps

Fig. 4 The locations of boreholes, piezometers, pressuremeter tests and the cross-sections



provided by the Algerian Institute of Cartography and Remote Sensing (INCT);

- **Remote Sensing Images:** Data from optical InSAR satellite images with a high resolution, acquired both pre-earthquake and post-earthquake. Pre-quake InSAR satellite images and post-quake images were used to identify slope failures caused by the shaking. These satellite images with a resolution of about $350 \times 350 \text{ m}^2$ from the European Spatial Agency (ESA) were acquired between July and August 2020, close to the occurrence time of the Mila earthquake. Google Earth satellite images with a resolution of about 1 m per pixel for pre- and post-quake were also compared and analyzed for the determination of the slope failure after the earthquake.
- **Geological Data:** Data pertaining to lithology, bedrock, and tectonic structure, obtained by digitizing a published geological map at a scale of 1:50,000 (Vila 1980);
- **Laboratory and in-situ geotechnical test data:** comprise data from 19 boreholes (B) with depths ranging from 17 to 80 m, 10 of which were equipped with piezometers (BP), and 12 MPT, noted BPr, as well as laboratory tests on undisturbed soil samples from boreholes for different depths in subsoil layers, conducted by LNHC in 2020 as a specific geotechnical investigation of the landslide. The lithological features of the landslide area, including composite material and thickness of lithological units, are described using data from boreholes, which are used to prepare simplified cross-sections indicating the lithological features of the studied area
- **The rainfall database:** The meteorological data cover a period of one year from the AinTin meteorological station, located near the landslide area and monitored by the National Agency of Water Resources (ANRH 2020). The dataset includes the daily, monthly, and annual measurements of rainfall for the period from 2019 to 2023.
- **Field Hydrogeological Monitoring Programs:** The field monitoring programs involved the inventorying of 15 water points (including 10 piezometers, 2 springs, and 3 wells) conducted and monitored by the LNHC in 2020 and the CGS in 2021 throughout the landslide area. Monitoring was conducted during the high-water period (December to June), with monthly assessments of groundwater levels. Through these programs, hydrogeological investigations determine the conditions related to groundwater levels, rainfall infiltration mechanisms, and their impacts on stability. Then, the relationship between cumulative rainfall and groundwater level fluctuations and their influence on stability was examined using piezometers installed along the sliding plane. These piezometers were monitored for the period from August 2020 to June 2021.
- **Field Investigation Data:** These include geomorphological, geological, and hydrogeological mapping of the land-

slide, covering parameters like morphology, typology, perimeter, geometry, deformations, lithology, thickness of lithological units, wells, water springs, water seepage, source, groundwater level, etc. The obtained co-seismic landslide inventory map, based on high-resolution remote sensing images, was complemented by three weeks of field investigations.

- **Seismic data:** the characteristics of the seismic event of August 7th, 2020 were recorded by several local digital accelerograph stations monitored and maintained by the CGS as well as numerous international seismological stations. The nearest seismic station to the El Kherba landslide is the Barrage Beni Haroun (BBH) station located at a hypocentral distance of 5 km. The distance between the landslide and the epicenter of the Mila earthquake is 14 km.

Detailed and complete inventory mapping of deep-Seated landslide

The establishment of landslide inventories and the exploration of their typologies and spatial distribution are indispensable tools for comprehending the spatial and temporal characteristics of landslides. This understanding is vital for assessing the evolution of the landscape and determining landslide susceptibility and risk. Various methods have been employed for landslide detection, as documented in studies by Keefer (2002), Lee and Sambath 2006, Harp et al. (2011), Guzzetti et al. (2012), Xu (2014a), Tian et al. (2019), and Bourenane et al. (2022). These methods include: (i) visual analysis of stereo-pair aerial photographs or/and high-resolution satellite ortho-images; (ii) visual analysis of high-resolution DEMs (such as LiDAR); (iii) analysis of InSAR multi-temporal radar images; (iv) automated processing of optical remote sensing images; and (v) on-site field investigations.

The study utilized a technique that involves the synthesis of computer GIS and remote sensing technologies for the visual interpretation of high-resolution satellite images on the GIS platform. This approach has been demonstrated to be effective for earthquake-triggered landslides. The accurate inventory map at a scale of 1:10,000 was prepared in ArcGIS using standard landslide mapping techniques based on the following steps:

- (1) *Visual interpretation of Interferometry Synthetic Aperture Radar (InSAR) satellite images* by (Fig. 5):
- (2) Processing of two Sentinel-1A InSAR images before (Fig. 5a) and after the earthquake (Fig. 5b) using Sentinel Application Platform (SNAP) V7.0 software for.
- (3) Determining deformation and displacement interferograms (Fig. 5c) generated by the earthquake.

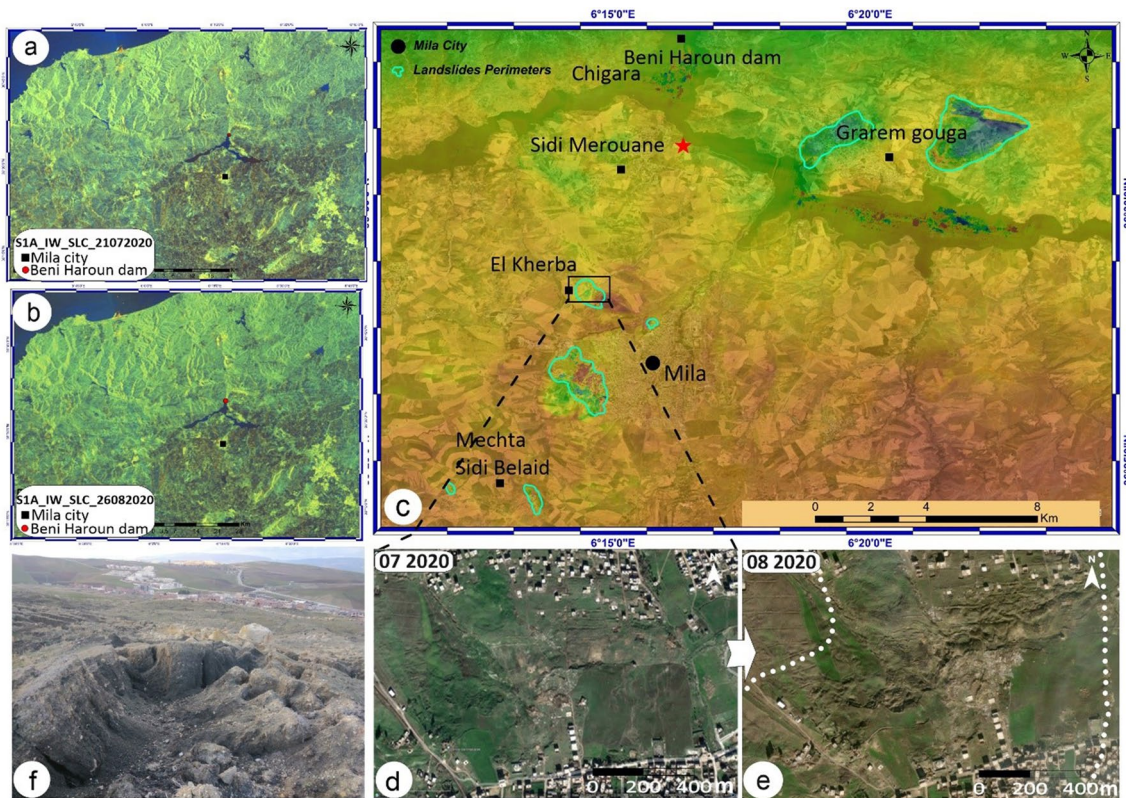


Fig. 5 Inventory mapping of the El Kherba landslide induced by the 7th August 2020 Mila earthquake based on the visual interpretation of pre- and post-earthquake remote sensing images derived from: (a) high resolution Interferometry Synthetic Aperture Radar (InSAR) satellite images of July 21, 2020, (b) InSAR satellite images of August 26, 2020, (c) the obtained interferogram from the processing of two

InSAR images (a) and (b); (d) and (e) Google Earth satellite images taken before (July 2020) and after (August 2020) the 2020 Mila Earthquake, respectively. (f) geomorphological field investigations. White dotted line are landslide boundaries of the El Kherba landslide. The red star indicates the Mila earthquake epicenter on August 7, 2020

- (4) Validating results with field geomorphological post-seismic investigation conducted shortly after the earthquake event;
- (5) Analysis and interpretation of Google Earth satellite images by:
- (6) Examining by comparing high-resolution images (1 m), taken prior to (Fig. 5d) and following (Fig. 5e), the earthquake event to identify landslides.
- (7) Comparing pre- and post-earthquake images to highlight changes.
- (8) Examination of archive documents and available data by:
- (9) Reviewing technical reports from LNHC 2020 and CGS 2022.
- (10) Consulting published geological maps.
- (11) Analysis of geomorphological field investigations:
- (12) Utilizing main results from field investigations conducted after the earthquake.
- (13) Confirming visual interpretations with GPS points from field observations.

This integrated approach aims to enhance the accuracy of landslide inventories by combining remote sensing technologies, GIS analysis, and on-the-ground field observations.

Geomorphological field investigations

Field investigation, which comprises geomorphological mapping, geological mapping, and reconnaissance studies on the landslide site, was performed according to the guidelines for landslide investigation proposed by Crozier (2005). The first geomorphological field reconnaissance of the site was carried out immediately one day after the slope failure, on August 8, 2020. Supplementary and extensive field investigations between August and September 2020 have been conducted in the landslides area in order to (Figs. 1 and 7): (i) verify and validate the landslide inventory map produced by the interpretation of satellite images; (ii) identify the geological conditions of slopes, type of material involved in slope failures and thickness of slope materials; (iii) identify and map the geomorphological features (typology,

topography, the perimeter, sliding surface) and deformation characteristics (such as head scarps, fissures, tension, bulges, subsidence... etc.) and geometrical parameters including slope angle, length, elevation, length, and width of the landslide; (iv) investigate potential causal factors of the landslides; (v) understand of landuse practices including changes in vegetation, agricultural practices, urbanization leading to modifications of natural morphology, as an important causal factor of instability and (vi) geotechnical investigations. Field observations also include drilling, core sampling for laboratory testing, groundwater level measurements, and MPT measurements.

Geological, hydrogeological and geotechnical investigations

The geological, hydrogeological, and geotechnical investigations carried out in the landslide area provide comprehensive insights into the subsurface conditions, groundwater behavior, and soil properties.

Geological investigations are conducted through the use of mechanical boreholes equipped with continuous coring in order to identify the lithological features of the landslide area and the thickness of the lithological units. A total of 19 boreholes, labeled B1 to B19, were drilled along the entire landslide surface, reaching depths ranging between 17 and 80 m (Fig. 4). Mechanical boreholes with continuous coring were employed to extract samples, enabling the identification of lithological features and the thickness of lithological units. The information obtained from the borehole is utilized to create simplified cross-sections that illustrate the lithological configuration of the landslide area in various directions.

The hydrogeological investigations involved the analysis of groundwater levels and their effects on stability. This was done through the creation of a piezometric level map, which represents the average groundwater table during the high-water period (December to February). The map was established using Kriging interpolation based on data from 15 water points, including 10 piezometers, 2 springs, and 3 wells.

Geotechnical investigations, including mechanical boreholes with continuous boring, laboratory experiments, tests on undisturbed samples from boreholes, and in situ tests by MPT, are also performed in order to identify the lithological sequences of soil constituting the slope, their physico-mechanical properties, and to determine the failure depths of the sliding area. A total of 55 undisturbed borehole samples from different depths of the lithological formations were collected for geomechanical laboratory testing. These tests included determining the grain size distribution by washing technique (ASTM International D1140-17, 2017), dry unit weight, moisture content-dry density, degree of saturation, soil classification (ASTM D2487-17), and Atterberg

limits tests (liquid limit LL and plastic limit PL). The residual shear strength parameters of soils were determined by employing repeated non-drained direct shear (DS) tests and unconsolidated undrained triaxial tests according to ASTM D-3080. The consolidation and compressibility properties of the soil were determined using oedometer tests, with each experiment conducted in accordance with relevant ASTM standards. In situ tests using 12 MPT were performed at intervals of 2 m depth for each borehole (BPr1 through BPr12), with a depth of 30 m for all boreholes except one (BPr12), which had a depth of 16 m. The MPT, based on ASTM Standards D 4719-07 (2007), determined two crucial parameters: deformation or pressuremeter modulus (E_p) and pressure limit (PI). E_p and PI values were solely employed for identifying both the deformable soil associated with instability (failure zone) and the slip surfaces of the landslide. A statistical analysis of physical and mechanical parameters and the geotechnical characteristics of the unstable slope was determined, and the results are presented in Table 2.

Failure mechanisms analysis

The inclinometer is the most frequently employed monitoring technique for identifying the failure mechanism, especially the depth and internal structure of slope deformations (Borgatti et al. 2006; Macfarlane 2009; Massey et al. 2013). Nevertheless, it comes with the drawback of necessitating highly reliable installation and monitoring procedures on the one hand and extensive and prolonged measurements on the other. In our case, the inclinometer results obtained from a specific geotechnical study of a landslide conducted by LNHC are prone to confusion due to the disadvantages given above. They exhibit highly variable sliding surface depths, ranging from 1 to 78.5 m, despite the geological formations being homogeneous. Consequently, the inclinometer outcomes fail to provide a clear depiction of deformation or the sliding surface.

To enhance the characterization of the failure mechanism, especially in determining the geometrical characteristics of the unstable slope, we employed a combination of theoretical or empirical measurements from the literature with practical testing through MPT investigations, accompanied by numerical modeling. This integrated methodology offers a more comprehensive understanding of the slope failure mechanism, contributing valuable insights for future slope stability assessments and engineering interventions.

Empirical measurements of geometrical setting

For individual landslides, a database of geometrical measurements involving landslide area, volume, landslide length, and landslide width was conducted through a worldwide

literature search (Soeters and van Westen 1996; Guzzetti et al. 1999; Guzzetti et al. 2009). However, for certain landslides, not all the information was accessible. From the available database of terrestrial landslides, the empirical relationship between landslide area A_L (in m^2), and volume V_L (in m^3) was modeled through the lineaire equation $V_L = \varepsilon \times A_L^\alpha$, where ε and α are empirically calibrated scaling parameters (Guzzetti et al. 2009; Simonett 1967; Guzzetti et al. 2008; Korup 2005; Hafliðason et al. 2005). Despite the dispersion attributed to various types of slope failures, most of the relationships exhibit a similar trend, the different parameters introduced to evaluate landslide volume, and the different climatic, geological, and physiographic settings (Guzzetti et al. 2009).

In the study area, the volume of the El Kherba landslide was estimated using empirical relationships published in the literature, including those proposed by Simonett 1967, Cruden and Varnes 1996, Korup 2005, Hafliðason et al. 2005, Parker et al. 2011, Guzzetti et al. 2008, 2009, and Xu et al. 2015. This volume information was then used to characterize the failure mechanism and, more precisely, to determine the depth of the sliding surface using the relationship $V = \pi LdDdWd/6$, proposed by Cruden and Varnes 1996, where Ld : length, Dd : depth, and Wd : width.

MPT investigations of the deformation zone

The MPT stands out as a crucial in-situ in geotechnical engineering, providing the most accurate depiction of soil deformation behavior. It is considered one of the most important tests for determining various geotechnical properties, including stress–strain behavior, shear strength, shear modulus, soil deformability, and the over-consolidation ratio of subsurface layers. Recently, this method has proven to be highly effective in determining the failure depths of a landslide (Ağan and Unal 2013).

This part of the study aimed to evaluate the effectiveness of the MPT in determining both the deformation zone associated with a landslide and the depth of the slip surface. To achieve this objective, the weak zones identified as probable sliding zones through pressuremeter tests, were compared with the failure depths obtained from inclinometer measurements and empirical relationships sourced from the literature. The findings from this investigation carry practical implications for geotechnical engineering, providing valuable insights into the applicability and efficiency of the MPT for this specific purpose. Consequently, the results of the MPT were correlated and calibrated with the inclinometers, boreholes, geotechnical tests, and empirical relationships published in the literature. This comprehensive approach ensures a thorough evaluation of the MPT and its utility in characterizing landslide deformation zones and determining slip surface depths.

Numerical simulation

A series of numerical simulations were conducted to understand the failure mechanism of the slope, focusing on the evaluation of the effects of the earthquake, and rainfall (groundwater level) effects. The behavior of soil layers was modeled using the Mohr–Coulomb model to simulate the movement process of a landslide. The input parameters of the model, including DEM, ground water level, and soil test results, are shown in Table 1. The behavior of slopes under the effect of earthquake was analyzed using the limit equilibrium method and the finite element method. This approach satisfactorily models the heterogeneous and discontinuous characteristics of soil masses. The initial stress within the soil body was generated using GEOSLOP 2D gravity loading. The standard fixities were applied as the mechanical boundary conditions. Subsequently, variations in annual groundwater levels were analyzed to assess their impact on pore-fluid pressure development and the initiation of this landslide, recognizing groundwater fluctuations as a crucial factor contributing to unstable conditions. Consequently, the results, determined the relationship between seismic loading and pore water pressure for the studied slope. The procedure for modeling, includes handling terrain data and constructing a geometric model. The factors of safety (FS) were assessed using fully coupled flow- deformation analysis, wherein soil hydraulic and mechanical responses were calculated simultaneously. Mesh dimensions were determined through sensitivity analysis to ensure a higher mesh density in the sliding zone. Numerical analyses were conducted for one cross section (profile AA') across the affected area, as depicted in Fig. 4.

Results inspection

Deep-seated landslide inventory map: types, characteristics and deformation

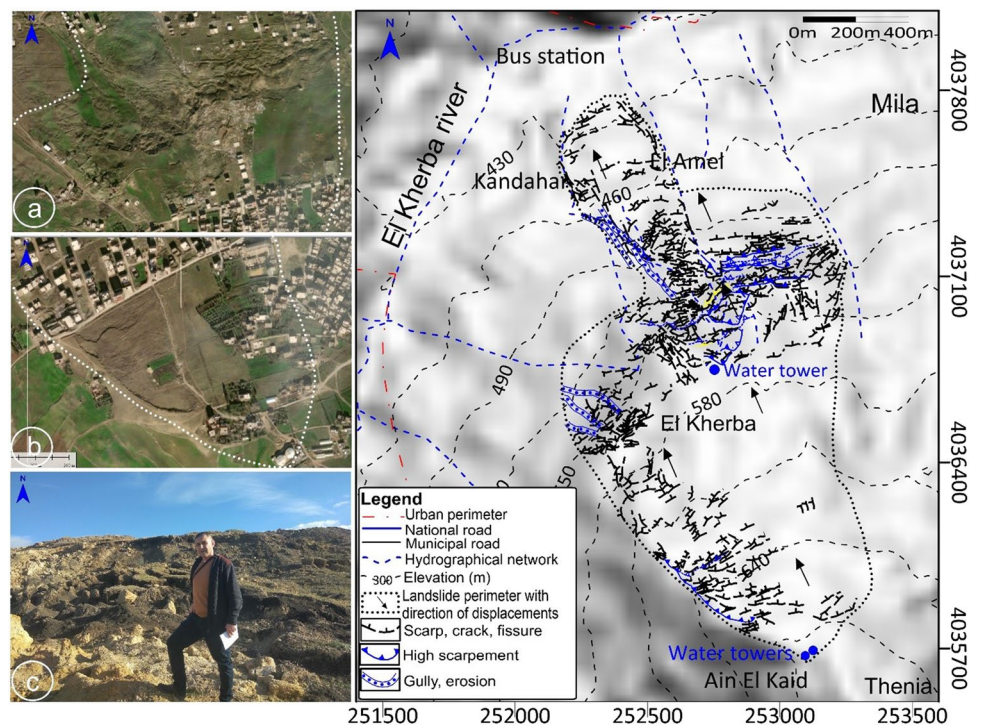
The inventory map of the El Kherba landslide has been established at a scale of 1:10,000 and is represented as polygons draped over a 10-m resolution DEM using Arc GIS (Fig. 6). The obtained inventory map outlines a large landslide, with an active zone covering a surface area of 1.565 km^2 . The entire length, spanning from the head scarp to the slope bottom, is approximately 2,166 km. The width across the landslide direction varies from 40 m to 1,80 km. This expansive landslide extends from the El Kherba district in the south to the Kandahar district and the El Amel districts in the north.

The mapped mass movement can be defined as a typical earth slide according to the classification of Varnes

Table 1 Descriptive statistics of the geotechnical properties of the soil samples

Geotechnical properties		Number of samples	Min. value	Max. value	Arithmetic mean	Standard deviation
Physical tests	Dry unit weight γ_d (kN/m ³)	14	15.3	18.5	17.05	0.080
	wet unit weight γ_h (kN/m ³)	14	18.3	21.3	20.24	0.064
	Moisture content ω (%)	26	10.07	24.47	17.002	3.316
	Degree of saturation S_r (%)	14	53.73	100	87.269	10.681
Atterberg limits tests	Liquid limit LL (%)	55	40.04	70.76	57.027	5.175
	Plastic limit PL (%)	22	22	42.42	29.465	3.183
	Plasticity index PI (%)	14	14.71	43	27.562	2.865
Drained direct shear (DS) test	Cohesion C (kPa/m ²)	37	10	51	33.4	0.071
	Internal friction angle ϕ (°)	11	11	40	18.216	4.284
Unconsolidated undrained triaxial test	Undrained Cohesion C_{uu} (kPa / m ²) (for dry season)	6	28.8	77.7	59.7	0.156
	Internal friction angle ϕ_{uu} (°) (for dry season)	2	2	5.4	3.55	0.933
The oedometer test	Coefficient of consolidation P_c (kPa)	37	95	213	143.7	0.269
	Coefficient of compressibility C_c (%)	11.33	11.33	32.64	18.505	3.688
	Coefficient of swelling C_g (%)	2.34	2.34	12.24	7.662	1.351
Manard pressuremeter test (MPT)	Deformation modulus E_p (MPa)	171	1.17	44.878	11.082	4.272
	Pressure limit P_l (MPa)	0.381	0.381	2.766	1.335	0.549

Fig. 6 Landslide inventory map of the El Kherba landslide area established at a scale of 1:10,000 based on: a) and b) analysis and interpretation of Google Earth/InSAR satellite images taken before and after earthquake event of August 2020 and completed and validated by c) extensive geomorphological field investigations. The white dotted points on satellite images are visible boundaries of the El Kherba landslide



(1978). The investigated landslides exhibit a trend along a NW–SE direction, with a height of 27.26 m from the road surface and a post-failure vertical angle of 63°. The studied

landslides trend along a NW–SE direction with a height of 27.26 m from the road surface and at an angle of 63° vertically post-failure.

The mass movement is complex, exhibiting characteristics of both a rotational landslide upstream and a translational landslide downstream, with several semi-circular scarps juxtaposed and two plane scarps, respectively. The slope is shifting towards the El Kherba river, with active peaks of rapid movement.

The geological mapping of the area showed that the El Kherba slope instabilities are very widespread, mainly within the thick series of sandy clays that belong to the post-nappe Miocene formation basin of Mila and along the 10° to 15° slopes (Fig. 6). Field observations indicate heavily weathered clays at the surface, crossed by a network of widely open retreating fissures, exposing them to concentrated runoff and erosion. Surface water infiltration through fissures and sandy layers causes progressive saturation, decompression of the formation, and the generation of interstitial overpressures, resulting in the loss of the mechanical properties of the soil.

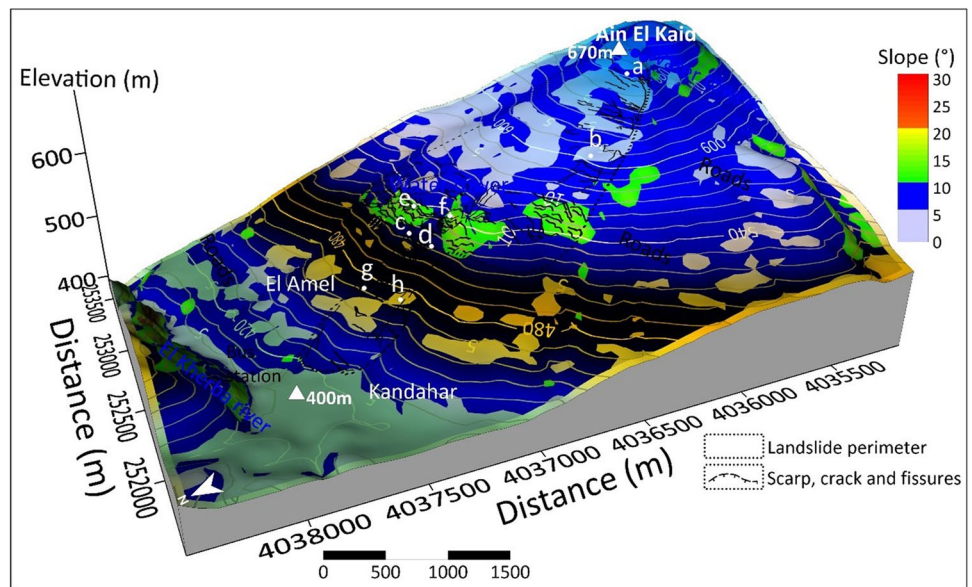
Morphological observations depict a disrupted landscape marked by numerous cracks, extensive depths, bulges, folds, and slope breaks, as illustrated in Figs. 7 and 8. Collectively, these features characterize an extensive, deep-seated landslide that has mobilized a considerable volume of slope material at a rapid velocity. The entire thickness of the overburden was displaced downslope and deposited on the right banks of the El Kherba River. The lower sections of the landslides display compression ridges, contributing to the displacement of structures. Furthermore, the residential buildings have incurred severe cracking, indicating a deterioration in the situation.

Many field observations in the landslide zone revealed the existence of previous evidence of instabilities and indicated that the landslides induced by the August 2020 earthquake event constitute partial reactivations of pre-existing landslides. The activation and reactivation of landslides in the Mila region are related to the intense rainfall events during the winter season.

Fig. 7 Field photographs showing the characteristics, types and, deformation characteristics of the El Kherba landslide: a) Main scarp near the water tank of Ain El Kaid, b) E-W oriented transverse cracks and escarpments developed downstream of the main scarp, c) Lateral escarpments oriented NW–SE marking the western limit of landslide at upper El Kherba, d) Large rectilinear lateral escarpment oriented NW–SE with a high horizontal rejection, e) A spectacular escarpment to the immediate north of the water reservoir marking the second main escarpment in the downstream of the landslide indicating ancient movements with a deformation characteristic, f) very extensive and height scarps in downstream related to the reactivated old landslide, g) and h) frontal bulges mobilising the dwellings in El Amel in the landslide toe. The locations of the photos (a-h) are shown on Fig. 9



Fig. 8 Local geomorphology and the relationship of the spatial distribution of the observed deformations with the slope angle on the digital elevation model. Letters (a–h) indicate the localization of photographs in Fig. 7



Geomorphological, hydrogeological and geotechnical conditions of the landslide

Local geomorphological characteristics

The El Kherba landslide was observed by residents 15 min after the seismic shock. It began with cracks, escarpments, and slight cracking on the walls and around some houses in the El Kherba district. By 10:00 p.m., the deformation intensified and moved in the northwest direction, passing through the Kandahar district and reaching the city of El-Amel, located 2 km downhill on the slope. The landslide is initiated on the upper part of the El Kherba hill facing SE NW at high to medium altitude. The affected area features a moderate to steep slope, dipping 10 to 30° to the Northwest. The landslide headscarp appeared near a municipality road and water tower, and the landslide toe is near the Mila bus station and El-Kherba river (Fig. 7). The head scarp of the landslide manifested near a municipality road and a water tower, while the toe of the landslide is situated close to the Mila bus station and the El Kherba River. The landform morphology has undergone significant changes due to slope instability, with numerous deformations observed along the entire landslide, extending from the main head scarp to the foot.

In the upstream parts of the landslide, a distinctive pattern emerges, characterized by a series of transverse cracks, tensile cracks, and bulges of varying depths and lengths running perpendicular to the slope direction. These features are separated by minor or secondary scarps. The landslide presents a main escarpment at the head of the landslide, more than 300 m long, oriented E-W (N 85°E) and observed to the immediate north of the small water reservoir of Ain El

Kaid, which supplies the town of Mila (Fig. 7a). This first semi-circular escarpment is followed by a series of transverse cracks and nested escarpments that develop downstream (Fig. 7b), the most important of which are almost rectilinear and oriented roughly E-W (N 120°E), limiting the semi-circular shape observed on the western side of the El Kherba slide (Fig. 7c).

A spectacular escarpment originates to the immediate north of the small water reservoir, still oriented roughly east–west (N 260°E), with a rejection this time of around 2 m (Fig. 7d). A municipality road along this escarpment collapsed with a vertical height of about 2.5 m and a distance of about 100 m.

In the downstream parts of the landslide, the deformations are very important because large and deep transverse cracks are observed with a width of 1 m to 6 m, a longitudinal length of ~ 150 m, and a depth of ~ 10 m (Figs. 7e and f). In this zone, very extensive and high scarps are also observed, with a longitudinal length of ~ 100 to 200 m and a rejection that can reach 5 to 15 m. These scarps form a slope break about 110 m long and 4 to 5 m high, which suggests that this zone corresponds to an old landslide reactivated in a versant with a higher slope. These landslides, which have been known previously, were triggered and reactivated by winter rainfall events. The downstream end of the landslides is marked by chaotic morphology, with frontal lobes and bulges mobilizing the dwellings in El-Amel (Figs. 7g and h) that correspond to the accumulation or depositional zone. In addition, this downstream zone is distinguished by human activities such as backfill surcharges and earthworks visible on satellite images (depicted in white in Figs. 5d and e). The spatial distribution of the observed deformations exhibits a clear correlation with the slope angle, as depicted in Fig. 8.

Geological characteristics

A cross-section derived from boreholes (Fig. 9) across the affected area (profiles AA', BB', and CC' of Fig. 11) reveals the lithological composition of the landslide. The predominant lithology consists of overlying Quaternary vegetal earths and backfill, underlying bedrock of the Mio-Pliocene formation composed of yellowish to greenish clays with some gravel, limestone, and gypsum banks at the surface. This is followed by greyish clays slightly marly in depth, featuring a layer of slightly clayey sand. The vegetal earth and backfill have a thickness ranging from 0.2 to 3 m and contain a small amount of sand and gravel. The bedrock slopes at an angle of 10 to 20 degrees to the northwest, aligning with the direction of the landslide. The borehole sections reveal the presence of both thin and thick (0.5–15 m) weak interlayers of altered and plastic clays with weak resistance,

especially at depths exceeding 6 m (Fig. 9). These strong plastic and weathered layer of clay with a narrow and muddy structure that reveal a soft layer with weak weathering resistance may constitute shear surfaces. This high plasticity is confirmed by the Casagrande plasticity tests (see “[Geotechnical properties: physical and mechanical parameters](#)”). Surface observations further reveal a thick deposit of clays with intercalations of sand and gray clay. This formation is often saturated, plastic, altered at the surfaces, and therefore sensitive to variations in water content. Consequently, it is extremely favorable to concentrated runoff, gully, erosion, and gravity-induced phenomena (Figs. 10 a and b).

Local hydrogeological characteristics

The upper layer of Miocene clays exhibits significant surface weathering, characterized by widely open desiccation

Fig. 9 Examples of the boreholes sections indicated the presence of thin and thick weak interlayers of altered and plastic clays

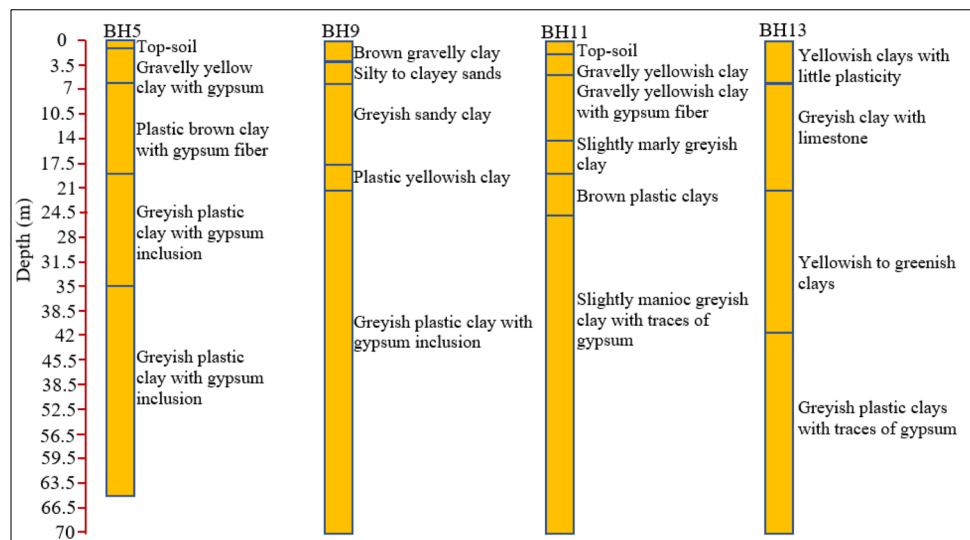


Fig. 10 Geological and hydrogeological characteristics of the clay Miocene formation: a) a weathered, plastic, loose, and porous, clays layer, observed at the landslide body with, a network of widely open shrinkage cracks, characteristics making them favorable for: b) surface water infiltration, concentrated runoff, gully, erosion and gravity phenomena. c and d): Groundwater discharge and water spring observed at the landslide toe after the earthquake event

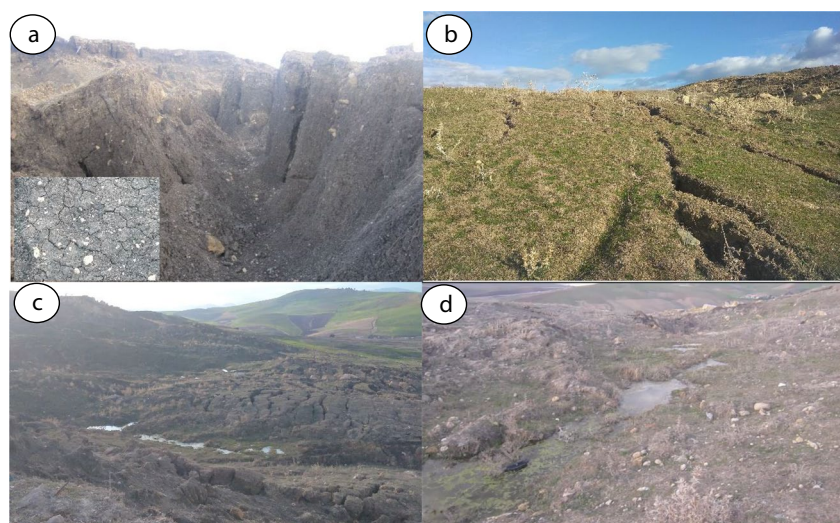
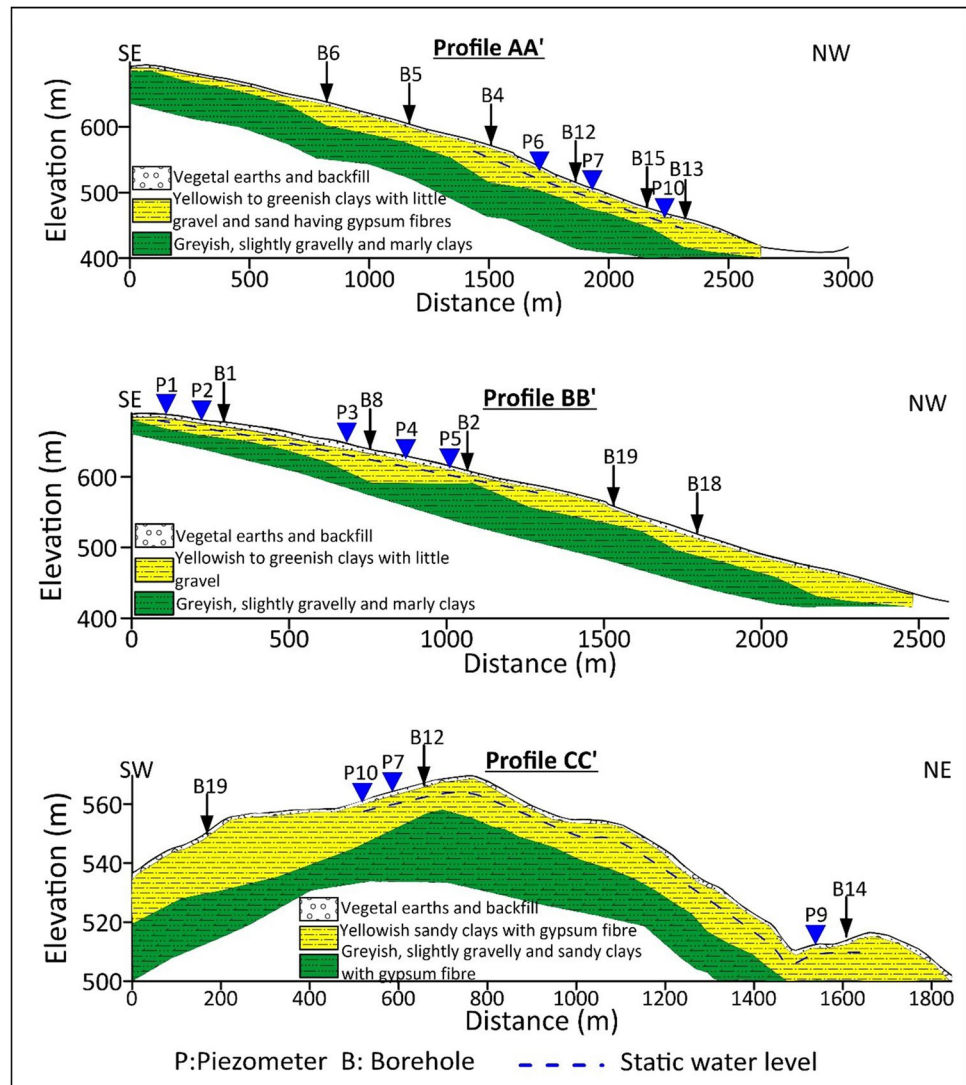


Fig. 11 Geological and hydro-geological cross-sections along the longitudinal and transversal profiles AA', BB' and CC' (locations of the cross sections is shown in Fig. 4) performed from boreholes and piezometers illustrating the lithological structure with static water level



cracks induced by shrinkage and swelling. This weathering renders the clays relatively permeable, enabling precipitation to infiltrate through the surface and contribute to the formation of a perched water table. This perched water table may play a role in the failure mechanism of the soils. During the rainy season, the groundwater level within the landslide rises. The majority of the water runoff and discharge follow the steep slope in a NW–SE direction toward the lower toe. Groundwater is then discharged, either as spring water at the foot of the steep slope in the lower part of the landslide or as seeps in a low depression at the lower part of the slope toe, as depicted in Figs. 10 c and d. The hydrological pattern plays a crucial role in influencing the dynamics of the landslide, particularly during periods of heightened rainfall.

The piezometric map, generated from data collected at 15 water points (including 10 piezometers, 2 springs, and 3 wells), reveals the presence of shallow to semi-deep groundwater, with a static water level ranging between

0.29 and 7.9 m. This groundwater, located within the clay deposits, is associated with soil saturation caused by the continuous accumulation of water, likely attributed to the infiltration of periodic winter rainfall. This type of groundwater manifests in the form of pellicular water tables, commonly known as perched water tables, within this particular coherent formation. The presence of perched water tables is indicative of temporary underground circulation at a relatively shallow depth. It's essential to note that while these estimated depths represent the maximum values, they may be minimal during wet seasons. The existence of a shallow water table increases the vulnerability of loose deposits in the area to sliding, particularly in the event of an anticipated earthquake. Figure 11 provides a depiction of the lithological structure of the landslide and the groundwater table in the landslide zone.

1) Influence of antecedent rainfall on landslides

The shallow water table is influenced by the antecedent or cumulative rainfall. However, the cumulative rainfall has influenced the degree of saturation of the soil and, consequently, played an important role in the initiation of landslides. Figure 12a shows the rainfall events registered by the local rain gauge, with indications of the duration (days), the maximum value of daily rainfall (mm), and the cumulated value of rainfall registered in the entire event (mm). The Mila region experienced prolonged and intense rainfall, with accumulative rainfall exceeding 250 mm, accounting for 55% of the total annual rainfall. The peaks of cumulated precipitation over one year ranged from the minimal 50 mm in January 2020 (54% of the annual amount) to the maximal 300 mm (97% of the annual amount). During the frequent and cumulative heavy rainfall, the infiltrated water increases the groundwater table level and the pore pressure, and decreases the effective stress of the soil, which reduces the shear strength of the material, resulting in slope failure. However, the pore pressure is influenced by the topography, hydraulic, and weathering properties of the soil.

2) Relationship between cumulative rainfall and groundwater level fluctuations

Understanding how rainfall influences groundwater levels in the examined slope is crucial, given that rainfall often serves as the main contributor to groundwater levels. The six piezometers BP1, BP2, BP3, BP5, BP8, and BP9 installed at the bottom of the boreholes along the sliding plane (Fig. 4), indicate a low fluctuation of groundwater level at a depth ranging between 2.5 and 7.9 m for the period from August 2020 to June 2021. Our realistic results show that a high value of groundwater level is observed during August 2020, corresponding to the period of groundwater discharge, and then the value increases from December to June, which corresponds to groundwater recharge (Fig. 12). A good correlation exists between typical cumulative precipitation (Fig. 12a) and groundwater level (Fig. 12b). The shallow depth of groundwater level is related to the saturation conditions caused by continual cumulative precipitation increasing the water content of the sliding mass, as observed after the earthquake event through sources and springs in the landslide toe (Figs. 10c and d), leading to a major loss in the shear strength of the sliding zone.

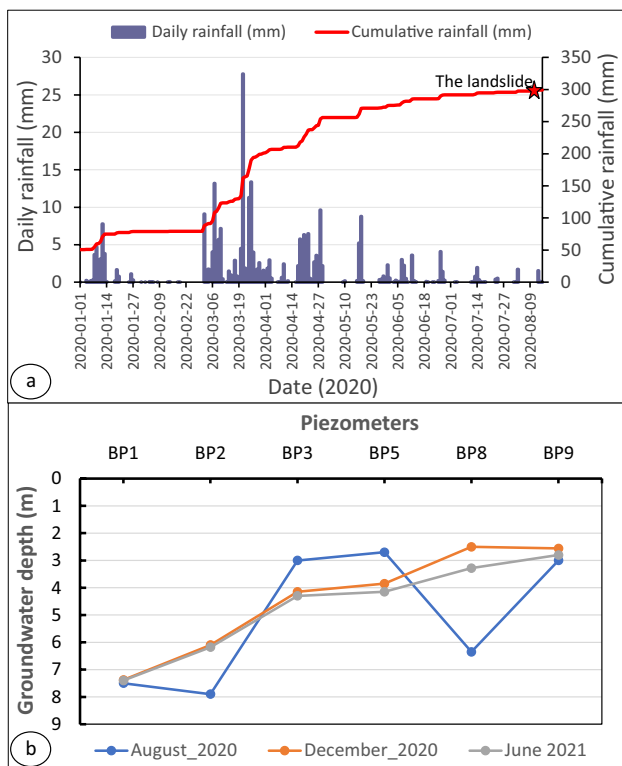


Fig. 12 Relationship between: a) Daily average and cumulative rainfall prior to the earthquake from January 1 to 15 August 2020 at the Ain Tin meteorological station in the city of Mila, and b) groundwater level fluctuations monitored by piezometers installed along the sliding plane for the period from August 2020 to June 2021. The red star marks when the El Kherba landslide and earthquake occurred

Geotechnical properties: physical and mechanical parameters

The LNHC conducted a geotechnical investigation to understand its behavior of the soil constituting the slope and to determine the geotechnical characteristics of the sliding area. The findings, including the number of samples taken for laboratory tests, as well as the mechanical and physical properties and statistical geotechnical parameters of the soils, are summarized in Table 1. Table 1 indicates that the physical and mechanical properties of the soil exhibit relatively small variations within a narrow range, as reflected in the low standard deviation values. This uniformity can likely be attributed to the geological homogeneity of the formations. Even though the characteristic properties of the formation are homogeneous, the mechanical properties of the samples from the deformation zone show significant differences. These values are nearly half of those observed in the other samples, suggesting a significant alteration in the soil properties within the landslide areas. This variation is believed to be a result of the soil in the landslide areas being disturbed by shear zones.

Grain size distribution The distribution of grain sizes significantly influenced the occurrence and frequency of landslides. In the landslide area, the soil's particulate size distribution was determined by utilizing regular sieves, fine sieves, and a hydrometer. Table 2 presents the statistical percentage of grain size distributions for the lithological unit.

Table 2 Grain size distribution of number of 45 samples in the lithological units

Grain size	< 80 μm (%)	Clay (%)	Silt (%)	Sand (%)	Gravel (%)
Min. value	53	33	12	6	0
Max. value	100	74	44	28	28
Arithmetic mean	91.968	63.867	19.556	13.167	3.588
Standard deviation	7.720	7.455	4.583	4.045	4.053

The analysis of grain sizes in samples taken at depths ranging from 1 to 80 m revealed cohesive soil, with over 50% of elements measuring less than 80 μm (fine fractions ranging from 53 to 100%). This indicates the presence of silty clay to sandy clays with the inclusion of gravel.

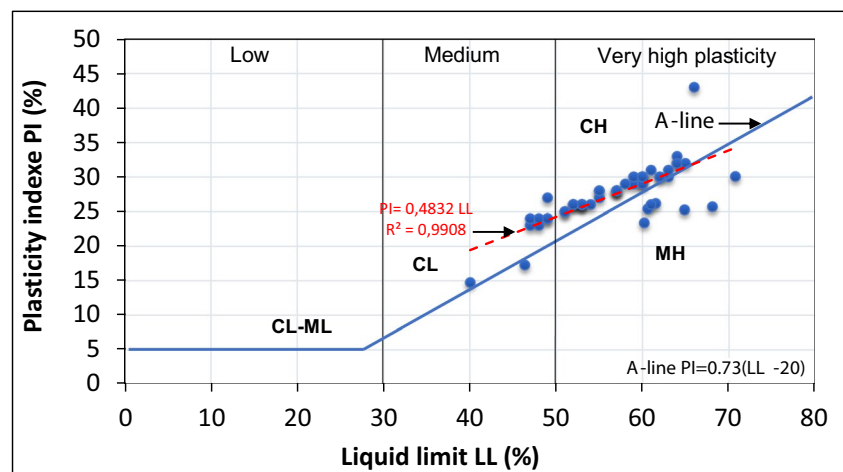
Plasticity characteristics: Atterberg limits and soil classification Fine-particle soil demonstrates the plasticity and cohesiveness required for reshaping without expansion or fragmentation. This distinctive characteristic depends on the quantity, mineralogical composition, and water content (moisture content) of the fines. In the presence of increased moisture content, clayey or silty soil becomes softer and stickier until it loses its ability to maintain its shape, transitioning into a liquid state. This shift is characterized by a reduction in the interaction between soil particles and the slurry, leading to the formation of a dispersion (Barnes 2000).

According to Casagrande's plasticity chart from 1936 (Fig. 13), the soils in question are identified as inorganic cohesive clays with high plasticity (CH), indicating a considerable capacity for volume changes. The majority of samples are positioned above the A-line, signifying liquid limits (LL) greater than 50% and a plasticity index (PI) exceeding 10. Notably, six samples fall below the A-line. Additionally, eight samples exhibit moderate plasticity. There is a discernible trend of increasing PI, best characterized by a linear relationship with LL ($R^2=0.99$). The liquid limits (LL) range from 40 to 71%, while the plastic limits (PL)

range from 22 to 42% (Table 1). The PI ranges from 15 to 43, indicating very high plastic soil and being very sensitive to the presence of water. The consistency index ranges from 0.94% to 1.63%, indicating firm to very stiff soils. Analysis of particle size distribution data reveals that the differences in plasticity among the samples can be largely explained by their higher sand fraction and relatively lower clay fraction, placing them in the category of medium plasticity. Both laboratory and field investigations indicate that the main contributing factor to the landslide was the altered and plastic nature of the soft soil.

Dry densities, wet densities and degree of saturation relation From the surface to the depths, the dry (γ_d) and wet densities (γ_h) range from 15.3 and 18.5 (kN.m^{-3}) and 18.3–21.3 (kN.m^{-3}), respectively, portraying a moderately dense state (Fig. 14). The natural water moisture content (ω) contents vary between 10 and 24.47%, while the degree of saturation (S_r) spans from 53.73% to 100% throughout the soil section. This indicates that the soil remains relatively wet, even in the dry season, owing to high atmospheric moisture. At depths ranging from 3 to 10 m, the clay exhibits dry and wet densities of 16.8–18.5 kN.m^{-3} and 20.2–20.8 kN.m^{-3} , respectively, characterizing the soils as dense. The average water content in this zone ranges from 12 to 15%. Notably, piezometric surveys have identified the presence of water at depths of 3 and 7.90 m. Finally, at depths exceeding 49.7 m, the dry and wet density values are low at 15.3 (kN.m^{-3}) and 18.3 (kN.m^{-3}). The corresponding moisture content and

Fig. 13 Atterberg limits of the samples on Casagrande Plasticity Chart. The dashed red line indicates a good linear relationship between PI and LL ($R^2=0.99$)



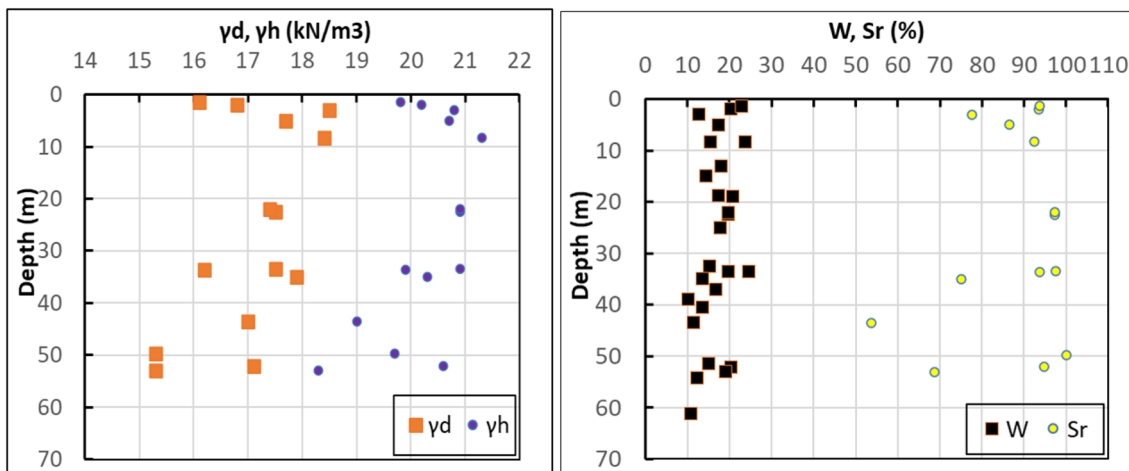


Fig. 14 Variation of γ_d , γ_h , W, and Sr values with depth

degree of saturation are high, with values of 15% and 100%, indicating a condition of low density and high saturation (Fig. 14).

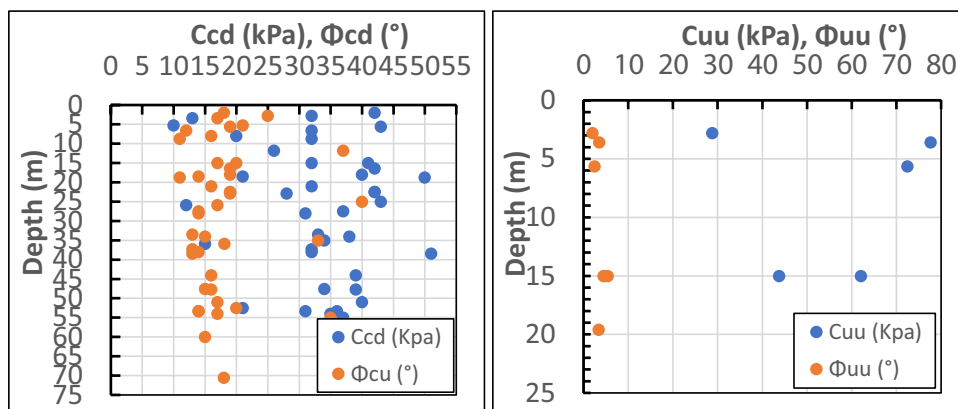
Shear strength parameter A landslide occurs when the soil surpasses the maximum shear stress it can withstand. Consequently, shear strength becomes a crucial parameter in understanding soil behavior. It is intricately linked to the soil's resistance to sliding along internal surfaces within the mass, making it a pivotal mechanical property in assessing landslide probability. The shear strength of soil is notably influenced by its water content, and most failures involve shear-type failures due to the movement of tiny soil particles when loaded. Key parameters defining shear strength include cohesion (c) and the internal angle of friction (ϕ) of the soil. The cohesion and angle of friction values are crucial factors in determining the shear strength of the soil, where higher values signify improved shear strength (Barnes 2000).

In this investigation study, shear strength properties (c and ϕ) were determined using the widely employed direct shear test and triaxial tests, suitable for all samples collected

during the dry season (Table 1). The results from the unconsolidated undrained triaxial test indicate that cohesion (C_{uu}) and internal friction angle (Φ_{uu}) of soil materials fall within the ranges of 28.8 to 77.7 kPa/m² and 2° to 5.4°, respectively, with averages of 60 kPa/m² and 3.55° (see Fig. 15). Conversely, in the consolidated drained test, these parameters range from 10 to 51 kPa/m² and 11° to 40°, with averages of 33.4 kPa/m² and 18.21°.

Results from the direct shear test reveal lower values of cohesion (C_u) and angle of friction (Φ_{cu}) in the range of 10 to 20 kPa/m² and 14° to 21°, respectively, for depths between 3 and 52 m. In contrast, depths of 25 to 60 m exhibit higher values, with $C_u > 31$ kPa/m² and $\Phi_{cu} > 18^\circ$. Notably, gravelly and sandy clays at depths of 3 to 5 m (boreholes B3 and B4) display low cohesion ($10 < C_u < 13$ kPa/m²), while plastic clays at a depth of 25 m (borehole B3) exhibit cohesion around $C_u = 10$ kPa/m². The presence of weak-resistance interlayers may contribute to the development of shear surfaces. The geotechnical characteristics of this soil suggest susceptibility to landslides, particularly local flows during earthquakes or heavy rainfall. The noted low residual

Fig. 15 Variation of the cohesion (c) and the internal angle of friction (ϕ) parameters values of a soil with depth



shear strength of the soils diminishes the resistance force of slope materials, consequently reducing the safety factor.

Consolidation, compressibility and classification The oedometer test reveals a coefficient of compressibility (Cc) ranging from 11.33% to 32.64%, indicating a relatively compressible soil. For the surface layer composed of sandy to gravelly clay, Cc values range from 12.49% to 24% at depths from 0 to 25 m (Fig. 16). Additionally, the coefficient of swelling (Cg) varies between 2.34% and 12.24%, classifying the soil as swelling. The values of consolidation pressure (Pc) range from 95 to 213 kPa, indicating an overconsolidated soil. In the case of altered brittle clays, the B3 survey at a depth of 60 m shows a Cc value of 32.64%, signifying a compressible soil, and a Cg value of 8.33%, suggesting potentially swelling soil. The consolidation pressure Pc = 164 kPa characterizes overconsolidated soil. The results from the oedometer test collectively indicate that the soils are compressible to highly compressible, overconsolidated,

and have the potential for swelling. The MPT test further reveals a deformation modulus varying between 1.17 MPa and 45 MPa, with an average of 11 MPa, and a pressure limit (Pl) ranging from 0.38 MPa to 2.76 MPa, with an average value of 1.33 MPa. These values clearly indicate the presence of soft clay."

Failure mechanism

The estimation of the deformation mechanism in the unstable area at El Kherba was derived through a combination of theoretical insights obtained from literature and practical testing, specifically pressuremeter tests and numerical simulations. These tests were employed to gauge the geometrical characteristics of landslides.

Geometrical setting of landslide

In the study area, the volume of the El Kherba landslide was estimated using empirical relationships from various sources in the literature (Table 3). This volume information served several purposes: (i) calibration of test results with available data; (ii) particularly calibration of test results for the depth of the sliding surface obtained from inclinometers; and (iii) characterization of the failure mechanism, specifically the internal structure of slope deformations. The obtained results indicate that the volume ranges from 36 169 461 m³ to 70 215 070 m³, with an intermediary value around 43 000 000 m³. Using these results, the depth of the sliding surface (Dd) was determined from the relationship $V = \pi LdDdWd/6$ of Cruden and Varnes (1996), where Ld represents length, Dd represents depth, and Wd represents width. The obtained Dd values range from a minimum of 25 m to a maximum of 48 m, with an average of 40 m (Table 3). According to the classification by Cruden and Varnes (1996), these results suggest a deep landslide. However, these results are

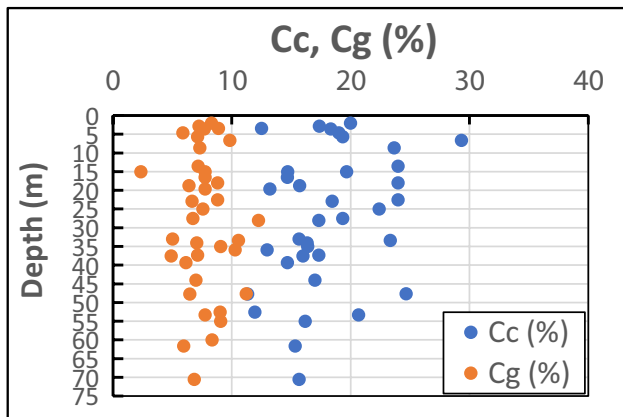


Fig. 16 Variation of the consolidation and compressibility parameters with depth

Table 3 Estimation of the geometrical characteristics (volume and depth) of the El Kherba landslides using empirical relationships available in the literature

ID	Equation	Volume V (m ³)	Depth of sliding surface Dd = 6 V / πLdWd (m) (Cruden and Varnes 1996)	Source
1	$V_L = 0,1479 \times A_L^{1,368}$	43 600 425.282	30.295	Simonett (1967)
2	$V_L = 12,273 \times A_L^{1,047}$	37 248 367.917	25.881	Haffidason et al. (2005)
3	$V_L = 0,00004 \times A_L^{1,95}$	47 298 169.139	32.864	Korup (2005)
4	$V = 0,106 \times A_L^{1,388}$	41 557 732.743	28.876	Parker et al. (2011)
5	$V_L = 0,0844 \times A_L^{1,4324}$	62 312 681.381	43.297	Guzzetti et al. (2008)
6	$V_L = 0,074 \times A_L^{1,450}$	70 215 069.577	48.788	Guzzetti et al. (2009)
7	$0.146 \times A_L^{1,332}$	25 784 909.238	17.916	Larsen et al. (2010)
8	$V = 1,0897 \times A_L^{1,2148}$	36 169 460.866	25.132	Xu and Rutledge (2016)

A_L landslide area, V_L volume, L_d length, D_d depth, W_d width

inconsistent with inclinometer measurements, which indicate a depth of the failure surface ranging from a maximum of 78.5 m to a minimum of 1.5 m. The inclinometer results are deemed unreasonable, suggesting an incomparable depth of the sliding surface in the three zones of the landslide (head, median, and accumulation).

Deformation zone determination using MPT

As illustrated in Fig. 17, the results of the E_p and P_l values exhibit comparability, indicating relatively low variations across all boreholes with homogeneous deformations. This consistent behavior can be attributed to the geological homogeneity of the formations under study. The findings consistently reveal that the deformation modulus of the soil mass increases proportionally with its depth. Within the database, the minimum deformation modulus (E_p) is recorded at 1.17 MPa, while the maximum value reaches 44.878 MPa. The values of the pressure limit (P_l) vary between 0.38 and 2.766 MPa. Most measurements of E_p range between 5 and 15 MPa. The testing depths, ranging from a minimum of 16 m to a maximum of 30 m, are almost uniformly distributed. Based on the results of E_p and P_l , the soil is classified as very soft according to Algerian seismic regulations (RPA 2003).

To ascertain the probable sliding surface depth using the MPT, weak zones (deformation zones) characterized by low values of P_l were identified and subsequently connected to one another to form a continuous plane. This connection was established by aligning the pressuremeters in the NW–SE landslide direction (Fig. 4). The outcome of this process was the determination of a specific plane based on the results of the MPT, as depicted in Fig. 17.

The connection between the pressuremeters was conducted following the alignment of the pressuremeters

in the NW–SE landslide direction. As a result of this process, a specific plane was determined based on the results of the MPT. The hypothesis is that the movements contributed to a reduction in the strength of this particular zone. Despite the characteristic properties of the formation being similar, variations in strength values were noted. The pressuremeter results indicate a deep deformation, with the sliding surface situated at a depth ranging from 10 to 15 m along the clay bedrock. Moreover, the rupture surface is positioned below the water table level. Furthermore, as illustrated in Fig. 18, the possibility of multiple superimposed failure surfaces cannot be dismissed. These surfaces may extend to a depth of 25 m, indicating composite sliding with several sliding surfaces superimposed.

The results from the pressuremeter tests demonstrated a close correspondence between the sliding surface (deformation zone) identified in the El Kherba landslide and the failure depths calculated using empirical relationships outlined in existing literature. In addition, the results obtained from laboratory tests confirm, validate, and support the findings from the field tests. The physical and mechanical properties of the deformation zone approve the presence of a plastic, saturated, weak-resistant, and overconsolidated soil with high compressibility and a significant potential for swelling. This observed variation is believed to be attributed to the shear zone, which induces soil degradation in faulty sections. Further evidence from boreholes indicates the presence of both thin and thick, weak interlayers composed of altered and plastic clays with low shear strength characteristics. Moreover, the frequent earthquakes in the area are identified as additional contributing factors to the observed deformation.

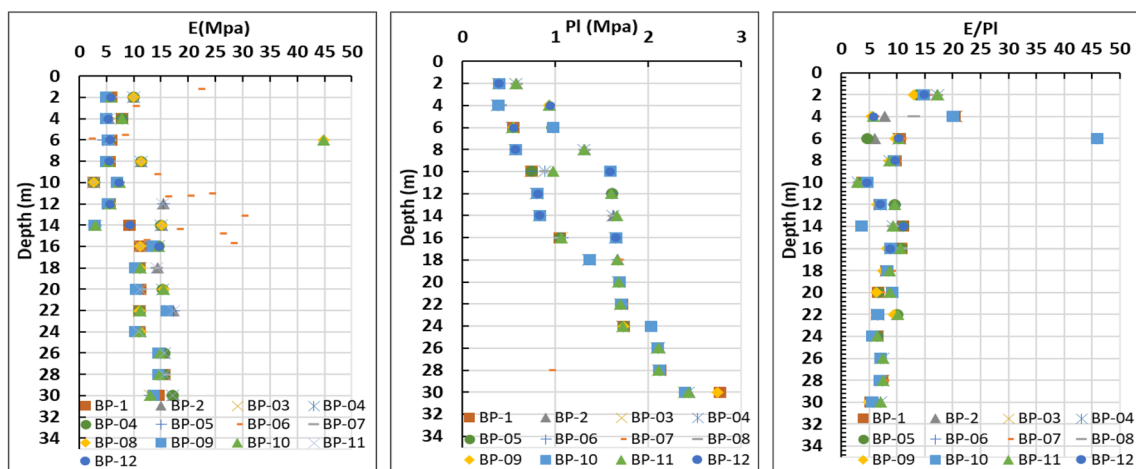


Fig. 17 E_p , P_l and E_p/P_l values from pressuremeters tests

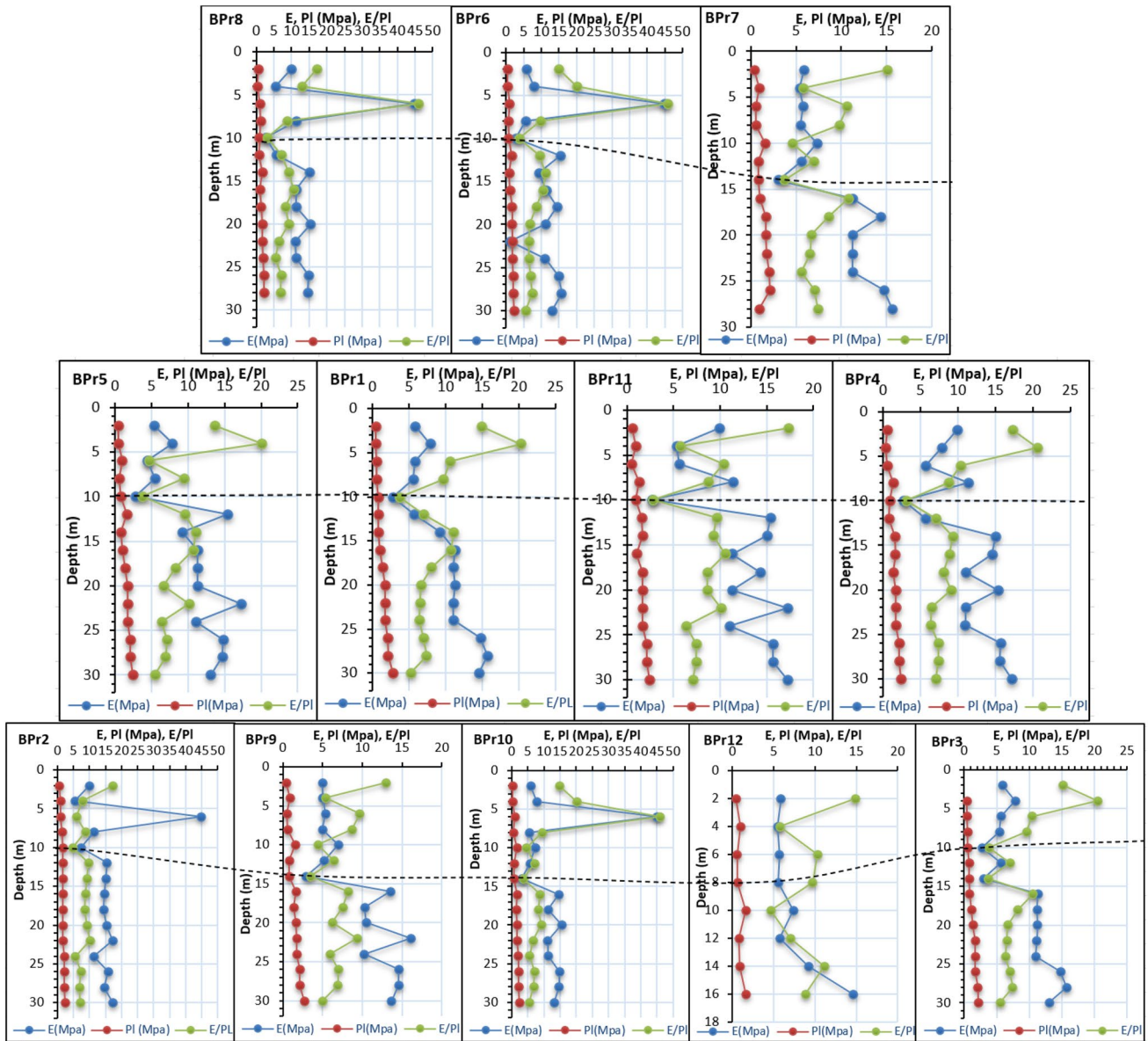


Fig. 18 The connection between the pressuremeters following the alignment of the pressuremeters profiles. The black dotted points indicate the probable slip surface

Numerical results

For numerical modeling, the recorded acceleration of the seismic event was applied to the slope model. The acceleration time histories used were recorded at the nearby BBH seismic station which is located at a hypocentral distance of 5 km. The N-S and E-W horizontal acceleration peaks (PGA), are significant, reaching a value of 0.23 g during the earthquake. While the vertical acceleration peaks (PGA) reached 0.24 g, slightly exceeding the horizontal acceleration. The acceleration was applied to the numerical model in the horizontal direction. Furthermore, the horizontal peak ground acceleration near the surface of the landslide

is greater than that at depth (Fig. 19). After configuring the model’s input parameters, deterministic analyses were performed to determine the slope stability associated with the combination of earthquake and rainfall. The numerical simulation analyzes the probability of failure (FS) of the slope related to the changes in the pore water pressure caused by groundwater level (rainfall) and earthquake. The factors of safety (FS) and sliding surfaces were depicted before and after the earthquake for section AA' (Fig. 20). The results illustrate that the mean value of FS was greater than 1.5 before the earthquake. However, the mean value of FS decreases to less than 1.5 after the earthquake. The results demonstrate that the groundwater level led to an increase in

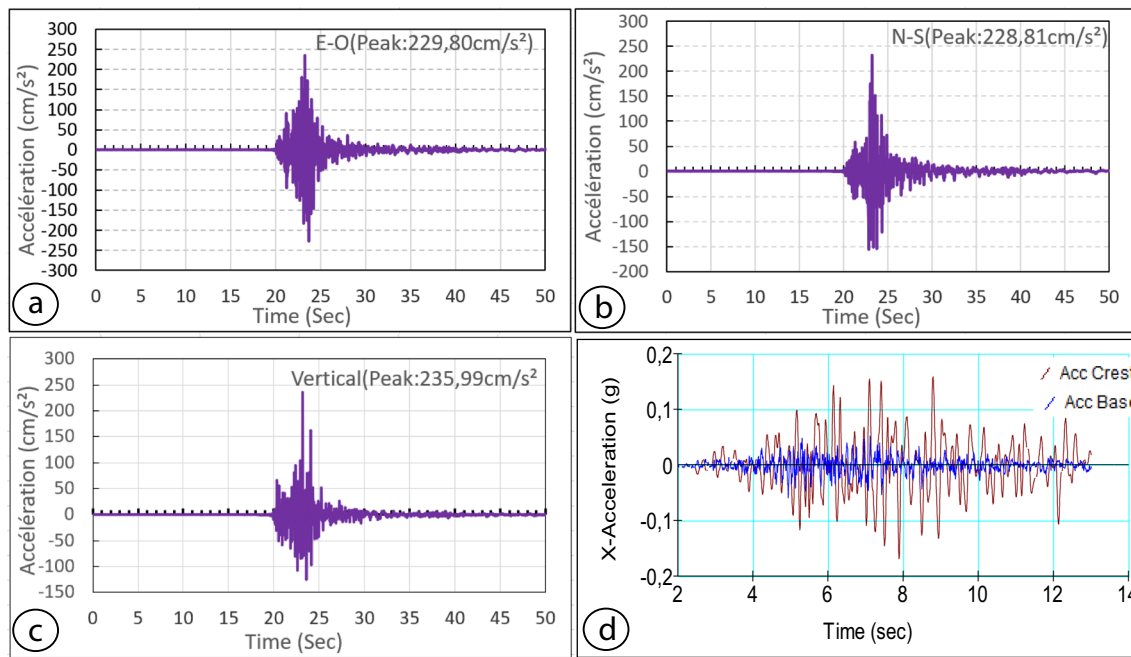
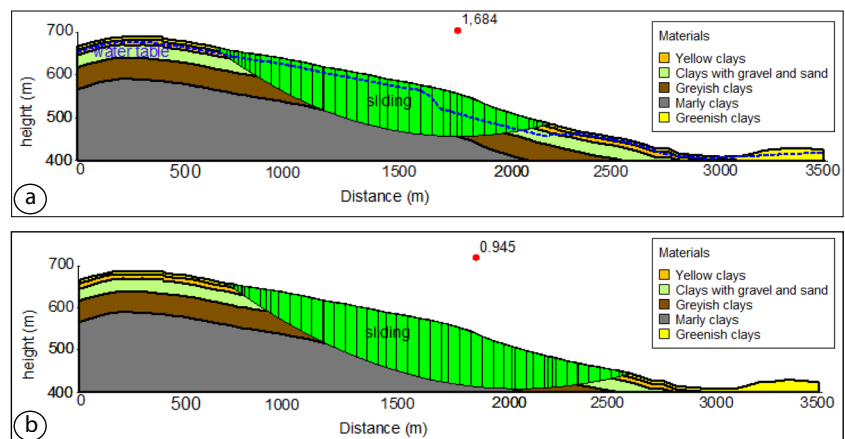


Fig. 19 Seismic records from the BBH seismic monitoring station during the Mila earthquake: (a) accelerations in east–west (EW), (b) north–south (NS) and in (c) vertical directions, respectively, (d) Amplification input (horizontal direction) used in the numerical simulation

Fig. 20 The numerical simulation results depict the safety factor (Fs) and the sliding surface of the selected cross section: a) before and b) after the earthquake



the pore water pressure ratio and a decrease in the factor of safety by approximately 1.48 times. The pore water pressure ratio increased from 0 before and during the earthquake to 0.286 (Fig. 21), with the factor of safety (FS) value reduced from 1.684 to 0.961. When the pore water pressure ratio reached its high value, the FS value decreased from 1.684 to 0.945. Additionally, the analysis results revealed that the studied slope initiated to instability around 7:30 a.m. on August 7th (after earthquake), when the FS value dropped below one. Subsequently, when the pore water pressure ratio reached its maximum value (Fig. 21), the deformations intensified and propagated over a distance of 2 km towards the downstream part by 10:00 p.m. The variation in pore water pressure caused by precipitation and its influence on

instability is really effective. These findings are consistent with those obtained from field observations. Consequently, landslide occurrences are inevitable in this area following rainfall and earthquake. The potential slip surfaces shown in Fig. 20 indicate that the entire study area is susceptible to deep sliding. As a result, structures located in this area along section AA' experienced significant deformations, reaching near-collapse and collapse levels, as observed from the damages incurred after earthquake, where the lowest FS (= 1) has been obtained from numerical analysis. Numerical simulations suggest that failure is likely to occur within the deep part of the landslide under earthquake conditions. These results are in accordance with those obtained from pressuremeter tests and empirical measurements (Fig. 22).

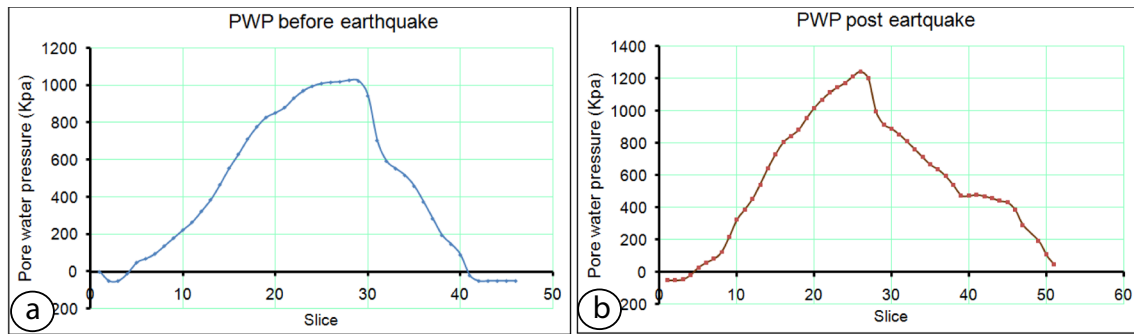


Fig. 21 The numerical simulation results depict the evolutions of pore water pressure ratio in the process of landsliding: a) before and b) after the earthquake

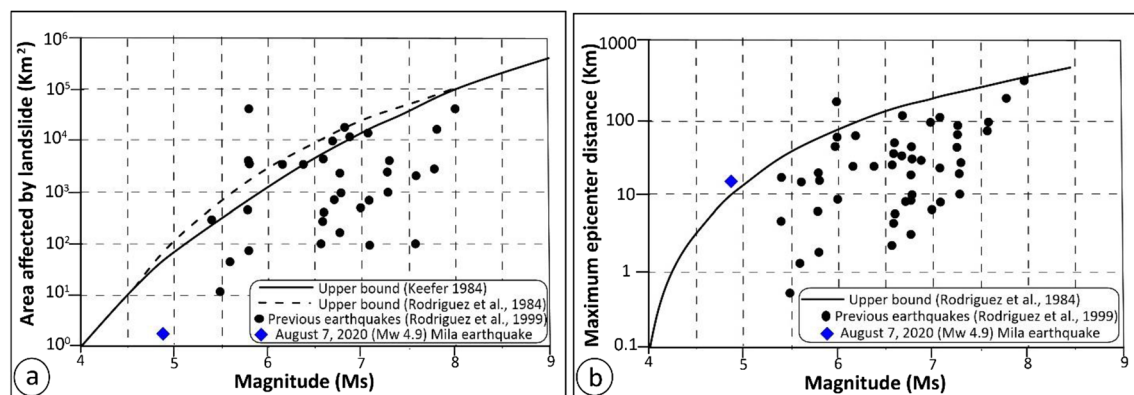


Fig. 22 Comparison of the distribution areas of coseismic landslides induced by the August 7th, 2020 (Mw 4.9) Mila earthquake with coseismic landslides worldwide: (a) Comparison of area affected by coseismic landslides with upper bound limits of Keefer (1984) and Rodriguez et al. (1999) and (b) comparison of maximum epicen-

tral distance to coseismic landslides with the upper bound of Keefer (1984) and data of Rodriguez et al. (1999). Data from Keefer (1984) are from coseismic landslides events occurred before 1980, and from Rodriguez et al. (1999) are from earthquake events occurred from 1980 to 1997

The arrival time of the mainshock is approximately 15 s, and its duration is about 30 s. The majority of the seismic energy is released within the first 20 s, causing slope loading without immediate instability due to the earthquake's short-duration movement. The initial deformations were observed in the upstream part of the slope 15 min after the seismic shock. Subsequently, the deformations intensify and propagate towards the downstream part, moving downhill along the slope after nine and a half hours. As time progresses, the velocity of the sliding body gradually diminishes due to the decreasing intensity of the earthquake and the dissipation of energy. This includes friction energy, collision energy, and deformation between the inter-particle system and particle–wall system, as well as a decrease in the pore water pressure ratio. \

Discussion and conclusion

Deep-seated disastrous landslides characterize substantial and rapid movements of earth and rock, often involving rock avalanches, with the potential to cause widespread devastation. These events are frequently triggered by severe earthquakes, inducing numerous mass movements of various sizes. The intricacy of large, deep-seated landslides is reflected in the challenge of identifying their crucial pre-failure conditions and predicting future actions. This poses a significant concern for scientists. In recent studies, multiparameter monitoring, physically based models, landslide geotechnical analysis, and landslide inventory mapping using field geological survey and remote sensing technology have emerged as valuable and

promising approaches enabling improved qualitative and quantitative analysis of landslides, especially on a larger scale (Tang et al. 2016; Su et al. 2017; Huang et al. 2018; Huang et al. 2018; Dai et al. 2019; Li et al. 2020; Chen et al. 2021; Zou et al. 2021; He et al. 2021; Xia et al. 2021; Bourenane et al. 2022; Bahmani et al. 2022; Ke et al. 2023; Dong et al. 2022). However, these multi-combination reconnaissance methods, require comprehensive data on geological structures, groundwater conditions, and geotechnical properties for accurate predictions and effective assessment of landslide susceptibility.

The present study employs a highly recommended approach for large-scale areas and provides detailed, accurate, and comprehensive inventory mapping and geotechnical characterization of large and deep landslides under various geomorphological and geological conditions. This objective is achieved through methodologies based on detailed geomorphological field investigation, satellite image interpretation, deep boreholes equipped with piezometers, laboratory tests, and in situ tests. The obtained results not only enhance our understanding of identifying and mapping complex landslides induced by earthquakes but also contribute valuable insights for reducing landslide hazards.

The obtained inventory map indicates that the entire active zone covers a surface area of 156,5 hectares, extending over approximately 2,166 km in length, with a width varying from 0.40 to 1.80 km. This landslide is classified as an earth slide type, involving a large and thick earth mass of clay moving down a slope. Geomorphological field mapping revealed a large and deep-seated morphological deformation related to: (i) the low stability slopes that the seismic strengths reducing the shear strength of the soil; (ii) a partial reactivation of preexisting landslide deposits; (iii) Miocene clays at the surface highly weathered and intersected by a network of open retreating fissures; and (iv) the influential role of unplanned urbanization and uncontrolled urban expansion in the development of the slide.

The initiation and reactivation of the El Kherba large, deep-seated landslide resulted from a combination of long-term and short-term triggering factors (including antecedent rainfall and the earthquake) and a susceptibility factor such as geomorphological, geological, hydrogeological, and geotechnical characteristics.

Seasonal intense rainfall and the accumulation of rainfall over time are crucial factors in the increase in the water content and pore pressures of clayey-marl soil and are therefore the origins of both the initiation and reactivation of landslides. It seems that the slope mass movement was closely related to the amount of rainfall, where the monthly rainfalls (January to August) during the activation of the landslide (2020) were all greater than the average annual values. During the period before the earthquake event, repeated rainfall episodes were characterized by high-intensity cumulative

precipitation (as shown in Fig. 12). The cumulative peak rainfall reached 300 mm, which corresponds to the high-water level. The low depth of groundwater level determined from piezometers for this short period confirms its relationship with the cumulative precipitation that has highly influenced landslide initiation and reactivation in specific geological conditions. Furthermore, the presence of previous landslide deposits, combined with antecedent rainfall, contributed to the amplification of the large landslide event.

The effect of earthquake event on the initiation and failure of landslides in the study area is controlled by three main aspects, i.e., acceleration amplification, magnitude, and epicentral distance. The acceleration, frequency content, and amplitude of the seismic signal can influence the type of landslide. Higher accelerations and lower frequency signals can lead to deep-seated or large-scale landslides (Jibson et al. 1994). Figure 19 indicates that the Mila earthquake is characterized by high acceleration, high amplitude, high frequency, and a short duration. The magnitude of the earthquake has a positive correlation with the size of the resulting landslide. Larger earthquakes with higher magnitudes tend to trigger larger landslides due to the increased energy released. Despite the relatively small size of the Mila earthquake (Mw 4.9), the recorded horizontal and vertical acceleration peaks (PGA) are significant, and causing a large and deep-seated landslide. The observed PGA amplification effect in the El Kherba slope is due to the local morphological, geological, hydrogeological, and geotechnical conditions. In addition, the landslide inventory map resulting from the Mila coseismic landslide is compared with those relative to other earthquakes worldwide (Keefer 1984; Rodriguez et al. 1999) using two parameters (Fig. 20a): magnitudes and landslide area. The inventory carried out by Keefer (1984) and Rodriguez et al. (1999) indicates that, despite the wide dispersion of values, the area affected by slope movements is of the order of 2 km² for a magnitude of 4.9 and could reach nearly 500,00 km² for a magnitude of 9.2. Additionally, according to the area of the landslides in relation to the magnitude of the earthquake, the area of the landslides caused by the Mila earthquake (Fig. 20a) is also comparable to worldwide landslide-affected areas suggested by Keefer (1984) and Rodriguez et al. (1999). As the distance from the epicenter increases, the likelihood of landslides decreases. As illustrated in Fig. 20b, this landslide occurred 14 km from the epicenter, fall within the upper margin established using data from other worldwide earthquakes by Keefer (1984) and Rodriguez et al. (1999). Following Keefer (1984), at such a distance, an earthquake magnitude of $M_s \geq 5.5$ is required. This underscores the high susceptibility of the landslide-prone area in Mila. However, the area and type of induced landslide in a particular area depend on its distance from the seismogenic fault as well as the magnitude and depth of the earthquake.

Moreover, the bedding structure of the lower soil slope with a thin and thick interlayer of plastic and altered clays has a direct effect or influence on the rock slope's instability because it's easy for a shear-slipping surface to form along weak interlayers. In addition to the lithological site effect associated with the presence of weathered plastic deposits, the site is situated on a small hill characterized by a contrasted relief with breaks in the slope. This topographical configuration likely led to significant amplifications.

The distribution of grain sizes in soil or rock materials plays a crucial role in determining the behavior of landslide movements, particularly the subsequent increase in pore pressure following failure. Samples characterized by finer grain sizes or higher proportions of fine particles are more prone to failure and can retain elevated pore pressure as they move. This underlines the significant influence of grain size and fine particle content on the mobility and behavior of earthquake-induced landslides. Both experimental data and field inspections consistently point to the prevalence of landslides in areas with clayey soils containing silty (19%), sandy (13%), and gravelly (3%) inclusions. The presence of these inclusions within clayey soils contributes to instability and susceptibility to landslides in such areas. An increase in the amount of pulverulent grains, particularly with a higher sand fraction, can disrupt drainage, elevate pore water pressure, and disturb the stability of the masses, thereby increasing the likelihood of landslides, especially during events such as earthquakes or heavy rainfall. An increase in clay content tends to result in higher internal friction but lower cohesion. This combination can enhance the potential for landslides, as clay-rich soils may have higher internal resistance to shear due to increased friction but may lack the cohesive strength necessary to hold soil particles together.

Slope stability is predominantly governed by the friction angle (ϕ) of the soil, and in cases with minimal cohesion, sudden failure can occur. Exceeding critical moisture levels in the soil substantially elevates the risk of rapid movement and failure. To evaluate saturation levels and failure risk, the moisture content of the slope is commonly contrasted with the liquid limit values in the layers most prone to failure. This analysis helps gauge how close the soil is to becoming fully saturated, potentially leading to landslides. The observation that the natural moisture content (ω) is very close to the liquid limit value is noteworthy, particularly in a humid and rainy study area. The average liquid limit values in the study area ranged from 40 to 71%, while the moisture content varied from 10 to 24%. This indicates that landslides are more likely to occur after heavy rainfall. During these periods, the soil's water content may exceed the liquid limit, significantly reducing its stability. The progressive saturation of the soil with water, favored by the infiltration and deep seepage of spring water, resulted in a landslide following a period of heavy rainfall during the rainy season.

Shear strength is indeed a critical factor in landslides. Soils with high shear strength can effectively stabilize slopes and resist failure. Conversely, an unstable slope can lead to short-term or long-term consequences, depending on the shear strength of the soil. It's crucial to note that the shear strength of materials does vary with changes in water content. High water pressures are a major contributing factor to slope failures and most landslides in the Mila province during rainstorms. The increase in water pressure diminishes effective stress, consequently reducing shear resistance. In the study area, the soils demonstrated significantly low shear strength values when saturated with water. During the rainy season, the maximum values of effective cohesion and angle of friction were measured at 60 kPa/m² and 4°, respectively. In contrast, for the dry season samples, the maximum effective cohesion and effective angle of friction values were reduced to 33 kPa/m² and 18°, respectively. The noted decrease in strength during wet conditions is a key factor contributing to failures in the study area, especially during the rainy seasons.

Findings from undrained triaxial cyclic loading tests suggest a high potential for generating excess pore-water pressures in the material during seismic loading. The direct shear test further revealed that disturbed soils exhibited an average cohesion of 33 kPa/m² and internal friction of 18°, signifying poor structural and shearing strength, rendering the soil susceptible to re-occurrence. Additionally, the presence of weak-resistance interlayers may serve as shear surfaces. The results of the oedometer test indicate that the soils are compressible to highly compressible, overconsolidated, and possess the potential for swelling.

In this study, pressuremeter tests were employed to determine the depth of the deformation zone. A previous study (Agan and Unal 2013) highlights that landslide can diminish the strength parameters of the soil through which they occur. Thorough investigations were initiated to estimate the boundaries of the moving surface depths through the assessment of strength reduction along the borehole. To identify the deformation zone using pressuremeter tests, testing depths with low P_l and E_p values were connected (Agan and Unal 2013). The hypothesis was that this deformation zone could potentially represent the depth of the landslide. The results of the pressuremeter tests led to the identification of a specific area through this process. Subsequently, the probable depth of the deformation zone determined through pressuremeter tests was compared with depths obtained using empirical relationships from existing literature. Figure 17 illustrates that the depths of the deformation zone, as determined by MPT, aligned well with those calculated using empirical relationships found in the literature.

The laboratory test results align with the field findings, confirming the physical and mechanical properties of the samples within the deformation zone. The identified

characteristics depict a plastic, saturated, weak-resistant, and overconsolidated soil with high compressibility and a substantial potential for swelling. This variation is attributed to the shear zone, inducing soil degradation in faulty sections. The study reveals a deep-seated and large landslide exhibiting a complex failure mode. The upper part of the earth slope initially deformed due to its weak geotechnical characteristics and slid along its geotechnical interface. Notably, the MPT proved effective in estimating the depth of the sliding surface and understanding the slope failure mechanism. The slip zone identified through the pressuremeters coincided with the failure depths obtained from laboratory tests, and calculations using empirical relationships available in the literature. However, a primary limitation of this study is acknowledged, stemming from the limited number of inclinometer and pressuremeter boreholes, along with the quality of monitoring and measurements of the inclinometer. To enhance the reliability of future studies, it is advisable to increase the number of inclinometer boreholes and prolong monitoring.

The numerical simulations analyze the probability of failure of the slope related to the changes in the pore water pressure caused by rainfall and earthquake. They provide comprehensive information on the characteristics and the failure mechanisms of the El Kherba landslide. The results indicate that failure is likely to occur within the deep part of the landslide under earthquake conditions. These findings align with the results obtained from pressuremeter tests and empirical measurements.

As a result, the current findings are anticipated to make a noteworthy contribution to the existing literature, particularly considering the absence of references to prior attempts utilizing laboratory tests, pressuremeter tests, and field investigations to determine a failure mechanism, especially the location of a slip surface. This research is crucial for advancing our knowledge of landslide prediction and helping to establish effective strategies and measures for risk mitigation in areas susceptible to such geological events.

Acknowledgements We gratefully acknowledge the support of the Centre National de Recherche Appliquée en Génie Parasismique of Algiers (CGS), Algeria, for their support in this research. We also express our gratitude to the Ministry of Housing and Urban Development and LNHC Est (Laboratoire National d'Habitat et de Construction) of Constantine for providing valuable geotechnical datasets essential for this study. We express our sincere gratitude to the local residents of El Kherba for providing useful information for the field investigations. The authors express their gratitude to the respected Editor-in-Chief and the anonymous reviewer for their valuable time and constructive comments, which have significantly enhanced the quality of the manuscript.

Author contribution The manuscript was conceptualised and written and through the contributions of all authors: All authors read and approved the final version of the manuscript.

Data availability The data used in this research can be made available upon request from the corresponding author.

References

- Agan C, Unal M (2013) Performance of pressuremeter tests to estimate the position of the sliding surface : a case study in Zonguldak. *Turkey Geotech Test J* 36(4):584–591
- Agence Nationale des Ressources Hydriques ANRH (2020) Rainfall database covering a time-period starting from 2019 to 2023 from the Ain Tin meteorological station
- Amar B, Ahmed S, Youcef B, Abdenmasser S, Mustafa A, Hamid B (2021) The main events of the July–August 2020 Mila (NE Algeria) seismic sequence and the triggered landslides. *Arab J Geosci* 14:1894. <https://doi.org/10.1007/s12517-021-08301-x>
- Aoudia A, Vaccari F, Suhadolc P, Meghraoui M (2000) Seismogenic potential and earthquake hazard assessment in the Tell Atlas of Algeria. *J of Seismology* 4:79–98
- ASTM International. D1140-17 (2017) Standard Test Methods for Determining the Amount of Material Finer than 75- μ m (No. 200) Sieve in Soils by Washing. ASTM International, West Conshohocken, PA. <https://doi.org/10.1520/D1140-17>
- Athmania D, Benaissa A, Hammadi A, Bouassida M (2010) Clay and marl formation susceptibility in Mila Province. *Algeria Geotech Geol Eng* 28(6):805–813. <https://doi.org/10.1007/s10706-010-9341-5>
- Bahmani F, Fattahi MH, Sabzevari T, Haghghi AT, Talebi A (2022) Spatial-temporal analysis of landslides in complex hillslopes of catchments using Dynamic Topmodel. *Acta Geophys* 70(3):1417–1432. <https://doi.org/10.1007/s11600-022-00786-8>
- Barnes GE (2000) *Soil Mechanics Principles and Practice*. Palgrave, New York
- Beldjoudi H, Delouis B, Djellit H, Yelles-Chaouche A, Gharbi S, Abacha I. (2016) The Beni-Ilmane (Algeria) seismic sequence of May 2010: Seismic sources and stress tensor calculations, <https://doi.org/10.1016/j.tecto.2015.12.021>.
- Benouar D (1994) Material for the investigation of the seismicity of Algeria and adjacent regions during the twentieth century. *Ann Geophys* 37(4). <https://doi.org/10.4401/ag-4466>
- Borgatti L, Corsini A, Barbieri M, Sartini G, Truffelli G, Caputo G, Puglisi C (2006) Large reactivated landslides in weak rock masses: a case study from the northern Apennines (Italy). *Landslides* 3(2):115–124. <https://doi.org/10.1007/s10346-005-0033-9>
- Bougrine A, Yelles-Chaouche AK, Calais E (2019) Active deformation in Algeria from continuous GPS measurements. *Geophys J Int* 217(1):572–588
- Bouhadad Y, Nour A, Laouami N, Belhai D (2003) The Béni-Ouartilane-Tachouaft fault: seismotectonic of the Babors region. *J Seismolog* 7(1):79–87
- Bouhadad Y, Benhammouche A, Bourenane H, Ait Ouali A, Chikh M, Guessoum N (2010) The Laalam (Algeria) damaging landslide triggered by a moderate earthquake (Mw=5.2). *J Nat Hazards* 54:261–272
- Bounif A, Haesler H, Meghraoui M (1987) The Constantine (Northeast Algeria) earthquake of October 27, 1987: surface ruptures and aftershocks study. *Eart Plan Sc Let* 85:451–460
- Bourdeau C (2005) effets de site et mouvements de versant en zones sismiques : apport de la modélisation numérique. Thèse de doctorat de l'École des Mines de Paris. Pg. 266
- Bourenane H (2023) Landslide hazard mapping using temporal probability analysis of rainfall thresholds in the city of Azazga and surrounding areas, northern Algeria. *Arab J Geosci* 16:592. <https://doi.org/10.1007/s12517-023-11704-7>

- Bourenane H, Bouhadad H (2021) Impact of land use changes on landslides occurrence in urban Area: The Case of the Constantine City (NE Algeria). *Geotech Geol Eng* 39:1–21. <https://doi.org/10.1007/s10706-021-01768-1>
- Bourenane H, Braham M, Bouhadad Y, Meziani AA (2021) Spatial distribution, controlling factors and failure mechanisms of the large-scale landslides in the urban area of Azazga city (northern Algeria). *Environ Earth Sci* 80:313. <https://doi.org/10.1007/s12665-021-09607-5>
- Bourenane H, Bensalem R, Oubaiche EH, Braham M, Meziani AA, Tebbouche MY (2022) The Large Deep-Seated Landslide Induced by the March 12th, 2012 Rainfall Event in the City of Azazga, Northern Algeria: Deformation Characteristics and Failure Mechanisms. *Environ Earth Sci* 81:476. <https://doi.org/10.1007/s12665-022-10612-5>
- Bourenane H, Bouhadad Y, Guettouche M.S, Braham M. (2014) GIS-based landslide susceptibility zonation using bivariate statistical and expert approaches in the city of Constantine (North-east Algeria). *Bull Eng Geol Environ*. <https://doi.org/10.1007/s10064-014-0616-6>
- Bourenane H, Guettouche MS, Bouhadad Y, Braham M (2016) Landslide hazard mapping in the Constantine city, Northeast Algeria using frequency ratio, weighting factor, logistic regression, weights of evidence, and analytical hierarchy process methods. *Arab J Geosci* 9:154. <https://doi.org/10.1007/s12517-015-2222-8>
- Casagrande A (1936) The determination of the preconsolidation load and its practical significance. *Proc. 1st Int. Conf. Soil Mechanics and Foundation Engineering*, Cambridge, Mass USA 3:60–64
- CGS Centre National de Recherche Appliquée en Génie Parasismique (2022) Des campagnes piézométriques réalisées pour l'étude de Microzonage sismique de la ville d'Azazga. Unpublished Internal report
- Chen LC, Yang HQ, Song KL, Huang W, Ren XH, Xu H (2021) Failure mechanisms and characteristics of the Zhongbao landslide at Liuqing Village, Wulong, China. *Landslides* 18(4):1445–1457. <https://doi.org/10.1007/s10346-020-01594-1>
- Chen SL, Lin LK, Lin CF (2012) Landslide mechanism of Lincoln community disaster in Taipei. *Disaster Adv* 5(4):1729–1733
- Chettah W (2008) Investigation des propriétés minéralogiques et géomécaniques des terrains en mouvement dans la ville de Mila « Nord-Est d'Algérie » Mémoire de Magister en géologie, option géologie de génie civil et des milieux aquifères, Université Hadj Lakhdar, Batna Algérie. 157
- Chong X, Xiwei X, Xiyang W, Fuchu D, Xin Y, Qi Y (2013) Detailed catalog of landslides triggered by the 2008 Wenchuan earthquake and statistical analyses of their spatial distribution. *J Eng Geol* 21:25–44 ((in Chinese))
- Coiffait PE (1992) Un bassin post-nappe dans son cadre structural, exemple du bassin de Constantine (Algérie orientale). Thèse doctorat sc. Univ. Nancy, 502
- CRAAG Centre de Recherche en Astronomie, Astrophysique et Géophysique CRAAG (2020). The August 7, (2020) (Mw 4.9), Mila earthquake (northeastern Algeria). Unpublished internal report
- Cruden D.M, Varnes D.J (1996) Landslide types and processes. In: Turner, A.K., Schuster, R.L. (Eds.), *Landslides, Investigation and Mitigation*, Transportation Research Board Special Report 247, Washington D.C., 36–75.
- Dai FC, Lee CF (2002) Landslide characteristics and slope instability modelling using GIS, Lantau Island, Hong Kong. *Geomorphology* 42:213–228
- Dai FC, Dong WP, Huang ZQ, Lei JH, Zhang HY (2019) Jul. Deformation mechanism of Area C landslide in Suijiang, Xiangjiaba Reservoir, Yunnan Province China. *Desalin Water Treat* 157:209–218. <https://doi.org/10.5004/dwt.2019.23846>
- Dong JH, Qiu M, Zhao JJ, Li HJ, Wu QH (2022) Deformation instability mechanism of slope in Fa'er Town, Shuicheng County, Guizhou China. *Alex Eng J* 61(10):8289–8295. <https://doi.org/10.1016/j.aej.2022.01.042>
- Guemache MA, Machane D, Beldjoudi H, Gharbi S, Djadia L, Benahmed S, Ymmel H (2009) On a damaging earthquake-induced landslide in the Algerian Alps: The March 20, 2006 Laâlam landslide (Babors chain, northeast Algeria), triggered by the Kherrata earthquake (M_w 5.3). *Nat Hazards* 54:273–288. <https://doi.org/10.1007/s11069-009-9467-z>
- Guzzetti F, Carrara A, Cardinali M, Reichenbach P (1999) Landslide hazard evaluation: a review of current techniques and their application in a multi-scale study, Central Italy. *Geomorphology* 31:181–216
- Guzzetti F, Ardizzone F, Cardinali M, Galli M, Reichenbach P, Rossi M (2008) Distribution of landslides in the Upper Tiber River basin, central Italy. *Geomorphology* 96:105–122
- Guzzetti F, Ardizzone F, Cardinali M, Rossi M, Valigi D (2009) Landslide volumes and landslide mobilization rates in Umbria, central Italy. *Earth Planet Sci Lett* 279(3–4):222–229. <https://doi.org/10.1016/j.epsl.2009.01.005>
- Guzzetti F, Mondini AC, Cardinali M, Fiorucci F, Santangelo M, Chang K.-T (2012) Landslide inventory maps: new tools for an old problem. *Earth Sci Rev* 112(1–2):42–66
- Hadji R, Boumazbeur A, Limani Y, Baghem M, Chouabi A (2013) Geologic, topographic and climatic controls in landslide hazard assessment using GIS modeling: A case study of Souk Ahras region, NE Algeria. *Quat Int* 302:224–237
- Hafidason H, Lien R, Sejrup HP, Forsberg CF, Bryn P (2005) The dating and morphometry of the Storrega Slide. *Mar Pet Geol* 22:187–194
- Harbi A, Maouche S, Ayadi A (1999) Neotectonics and associated seismicity in the Eastern Tellean Atlas of Algeria. *J Seismol* 3:95–104
- Harbi A, Maouche S, Ayadi A, Benouar D, Panzag F, Benhallou H (2004) Seismicity and tectonic structures in the site of algiers and its surroundings: a step towards microzonation. *Pure Appl Geophys* 161(2004):949–967. <https://doi.org/10.1007/s00024-003-2502-1>
- Harbi A, Meghraoui M, Maouche S (2011) The Djidjelli (Algeria) earthquakes of 21 and 22 August 1856 (Io=VIII, IX) and related tsunami effects Revisited. *J Seismol* 15(1):105–129
- Harp EL, Keefer DK, Sato HP, Yagi H (2011) Landslide inventories: The essential part of seismic landslide hazard analyses. *Eng Geol* 122(1–2):9–21
- He X, Chong X, Qi Y, Yuandong H, Cheng J, Xiwei X, Yao Q, Yongkun L, Dai B (2021) Landslides Triggered by the 2020 Qiaojia Mw 5.1 Earthquake, Yunnan, China: Distribution, Influence Factors and Tectonic Significance. *Journal of Earth Science* 32(5):1056–1068. <https://doi.org/10.1007/s12583-021-1492-1>
- Huang RQ (2012) Mechanisms of large-scale landslides in China. *Bull Eng Geol Env* 71(1):161–170. <https://doi.org/10.1007/s10064-011-0403-6>
- Huang C, Li YS, Yi SJ, Wu C (2018) Characteristics and failure mechanism of an ancient earthquake-induced landslide with an extremely wide distribution area. *J Mt Sci* 15:380–393. <https://doi.org/10.1007/s11629-017-4527-4>
- Ke Z, Hong W, Liao JX, Zhang YG, Chen FP, Yang ZJ (2023) Deformation and failure mechanism of colluvial landslide under sustained rainfall—a case study of Xinzhan landslide in Tongzi County, China. *Alex Eng J* 71:89–103. <https://doi.org/10.1016/j.aej.2023.03.044>
- Keefer DK (1984) Landslides caused by earthquakes. *Geol Soc Am Bull* 95(4):406–421. [https://doi.org/10.1130/0016-7606\(1984\)95%3c406:LCBE%3e2.0.CO;2](https://doi.org/10.1130/0016-7606(1984)95%3c406:LCBE%3e2.0.CO;2)
- Keefer DK (2002) Investigating landslides caused by earthquakes—a historical review. *Surv Geophys* 23(6):473–510. <https://doi.org/10.1023/A:102127471>
- Kherroubi A, Deverchère D, Yelles A, Mercier de Lepinay B, Domzig A, Cattaneo A, Bracene R, Gaullier V, Graindorge D (2009) Recent and active deformation pattern off the easternmost Algerian margin, western Mediterranean Sea: New evidence of contractional tectonic reactivation. *Mar Geol* 261:17–32

- Korup O (2005) Distribution of landslides in southwest New Zealand. *Landslides* 2:43–51. <https://doi.org/10.1007/s10346-004-0042-0>
- Larsen JJ, Montgomery DR, Korup O (2010) Landslide erosion controlled by hillslope material. *Nat Geosci* 3:247–251
- Lee S, Sambath T (2006) Landslide susceptibility mapping in the Damrei Romel area, Cambodia using frequency ratio and logistic regression models. *Environ Geol* 50(6):847–856
- Li YL, Yao AJ, Gong YF (2022) Deformation and Failure Mechanism of a Massive Ancient Anti-Dip River-Damming Landslide in the Upper Jinsha River. *Sustainability* 14(20):13048. <https://doi.org/10.3390/su142013048>
- Li, W. L., Zhao, B., Xu, Q. & Wu X. X. (2020). Deformation characteristics and failure mechanism of a reactivated landslide in Leidashi, Sichuan, China, on August 6, 2019: an emergency investigation report. *Landslides*(prepublish). <https://doi.org/10.1007/s10346-020-01367-w>
- LNHC (2020) Étude géotechnique et de stabilité : site El Kherba-Mila. Unpublished Internal reports. Laboratoire national d'habitat et de construction
- Macfarlane DF (2009) Observations and predictions of the behaviour of large, slowmoving landslides in schist, Clyde dam reservoir. *New Zealand Eng Geol* 109(1–2):5–15. <https://doi.org/10.1016/j.enggeo.2009.02.005>
- Maouche S, Meghraoui M, Morhange C, Belabbes S, Bouhadad Y, Haddoum H (2011) Active coastal thrusting and folding, and uplift rate of the Sahel Anticline and Zemmouri earthquake area (Tell Atlas, Algeria). *Tectonophysics* 509:69–80. <https://doi.org/10.1016/j.tecto.2011.06.003>
- Maouche S, Bouhadad Y, Harbi A, Rouchiche Y, Ousadou F, Ayadi A (2019) Active tectonics and seismic hazard in the Tell Atlas (Northern Algeria): a review. In: Bendaoud A (ed) *The geology of the Arab world—an overview*. Springer Nature, 381–400. https://doi.org/10.1007/978-3-319-96794-3_10
- Massey CI, Petley DN, McSaveney MJ (2013) Patterns of movement in reactivated landslides. *Eng Geol* 159(12):1–19. <https://doi.org/10.1016/j.enggeo.2013.03.011>
- Meghraoui M (1988) Géologie des zones sismiques du Nord de l'Algérie. Paléosismologie, tectonique active et synthèse sismo-tectonique. Thèse doct. Univ. Paris VI, 356
- Parker RN, Densmore AL, Rosser NJ, Michele M, Li Y, Huang R, Whadcoat S, Petley DN (2011) Mass wasting triggered by the 2008 Wenchuan earthquake is greater than orogenic growth. *Nat Geosci* 4:449–452
- Pasierb B, Grodecki M, Gwozdz R (2019) Geophysical and geotechnical approach to a landslide stability assessment: a case study. *Acta Geophys* 67(6):1823–1834. <https://doi.org/10.1007/s11600-019-00338-7>
- Rodriguez CE, Bommer JJ, Chandler RJ (1999) Earthquake-induced landslides: 1980–1997. *Soil Dynamics Earthquake Engineering* 18:325–346
- RPA (2003) Algerian building code, RPA99/2003, DTR-B.C.2.48, Ministry of Housing and Urban Planning, Algeria
- Sato HP, Hasegawa H, Fujiwara S, Tobita M, Koarai M, Iwahashi J (2007) Interpretation of landslide distribution triggered by the 2005 Northern Pakistan earthquake using SPOT 5 imagery. *Landslides* 4(2):113–122. <https://doi.org/10.1007/s10346-006-0069-5>
- Shi GC, Yang XJ, Chen W, Chen H, Zhang JC, Tao ZG (2021) Characteristics of failure area and failure mechanism of a landslide in Yingjiang County, Yunnan China. *Landslides* 18(2):721–735. <https://doi.org/10.1007/s10346-020-01544-x>
- Shoaei Z (2014) Mechanism of the giant Seimareh Landslide, Iran, and the longevity of its landslide dams. *Environ Earth Sci* 72(7):2411–2422. <https://doi.org/10.1007/s12665-014-3150-8>
- Simonett DS (1967) Landslide distribution and earthquakes in the Bewani and Torricelli Mountains, New Guinea. In: Jennings JN, Mabbutt JA (eds) *Landform Studies from Australia and New-Guinea*. Cambridge University Press, Cambridge, pp 64–84
- Soeters R, van Westen CJ (1996) Slope instability recognition, analysis and zonation. In: Turner AK, Schuster RL (eds) *Landslide Investigation and Mitigation*. Transportation Research Board Special Report, vol. 247. National Research Council, pp 129–177
- Su LJ, Hu KH, Zhang WF, Wang J, Lei Y, Zhang CL, Cui P, Pasuto A, Zheng QH (2017) Characteristics and triggering mechanism of Xinmo landslide on 24 June 2017 in Sichuan China. *J Mt Sci* 14(9):1689–1700. <https://doi.org/10.1007/s11629-017-4609-3>
- Tang MG, Xu Q, Li YS, Huang RQ, Rengers N, Zhu X (2016) Partial reactivation of a huge deep-seated ancient rock slide: recognition, formation mechanism, and stability. *Nat Hazard* 16(8):1719–1735. <https://doi.org/10.5194/nhess-16-1719-2016>
- Tebbouche MY, Ait Benamar D, Hassan HM, Singh AP, Bencharif R, Machane D, Meziani AA, Nemer Z (2022) Characterization of El Kherba landslide triggered by the August 07, 2020, Mw = 4.9 Mila earthquake (Algeria) based on post-event field observations and ambient noise analysis. *Environ Earth Sci* 81:46. <https://doi.org/10.1007/s12665-022-10172-8>
- Tian YY, Xu C, Ma SY, Xu XW, Wang SY, Zhang H (2019) Inventory and spatial distribution of landslides triggered by the 8th August 2017 MW 6.5 Jiuzhaigou earthquake. *China. J Earth Sci* 30(1):206–217
- Varnes DJ (1978) Slope movement, types and processes. In: Schuster RL, Krizek RJ (Eds) *Landslides, analyses and control*. National Academy of Science, Report 176, Washington, DC, pp 11–35
- Vila JM (1980) La chaîne alpine d'Algérie orientale et des confins algéro-tunisiens. Ph.D thesis, Paris VI, 2 t., 665
- Wang YS, Luo YH, Li YS, Wu JF (2010) The genetic mechanism of Gangudi landslide. *Disaster Adv* 3(4):77–80
- Wang LQ, Lu S, Li CD (2012) Study on Formation Mechanism of Yangjiashan Landslide in Enshi City, China. *Res J Chem Environ* 16:102–107
- Wu, J. Q., Dai, F. C., Liu, P., Huang, Z. Q., & Wu, D. X. (2023). Study on groundwater table distribution of loess tableland in the South Jingyang tableland, Northwest China. *Acta Geophysica*, 16. <https://doi.org/10.1007/s11600-023-01087-4>
- Xia M, Ren GM, Yang XL (2021) Mechanism of a catastrophic landslide occurred on May 12, 2019, Qinghai Province China. *Landslides* 18(2):707–720. <https://doi.org/10.1007/s10346-020-01559-4>
- Xu C, Xu X (2014) The spatial distribution pattern of landslides triggered by the 20 April 2013 Lushan earthquake of China and its implication to identification of the seismogenic fault. *Chin Sci Bull* 59(13):1416–1424. <https://doi.org/10.1007/s11434-014-0202-0>
- Xu C, Xu X, Shyu JBH (2015) Database and spatial distribution of landslides triggered by the Lushan, China Mw 6.6 earthquake of 20 April 2013. *Geomorphology* 248:77–92. <https://doi.org/10.1016/j.geomorph.2015.07.002>
- Xu W, Rutledge SA (2016) Time scales of shallow-to-deep convective transition associated with the onset of Madden-Julian Oscillations. *Geophys Res Lett* 43(6):2880–2888. <https://doi.org/10.1002/2016GL068269>
- Zhang CY, Yin YP, Dai ZW, Huang BL, Zhang ZH, Jiang XN, Tan WJ, Wang LQ (2021) Reactivation mechanism of a large-scale ancient landslide. *Landslides* 18(1):397–407. <https://doi.org/10.1007/s10346-020-01538-9>
- Zhu L, Deng Y, He SM (2019) Characteristics and failure mechanism of the 2018 Yanyuan landslide in Sichuan. *China Landslides* 16(12):2433–2444. <https://doi.org/10.1007/s10346-019-01262-z>
- Zou Z, Tang H, Criss RE, Hu X, Xiong C, Wu Q, Yuan Y (2021) A model for interpreting the deformation mechanism of reservoir landslides in the Three Gorges Reservoir area, China. *Nat Hazards Earth Syst Sci* (2). <https://doi.org/10.5194/NHESS-21-517-2021>